

Physics-Informed Neural Compression of High-Dimensional Plasma Data

Gianluca Galletti¹ Gerald Gutenbrunner¹ Sandeep S. Cranganore¹ William Hornsby² Lorenzo Zanisi²
 Naomi Carey² Stanislas Pamela² Johannes Brandstetter^{1,3} Fabian Paischer^{1,3}

⌚ ml-jku/neural-gyrokinetics 😊 gerkone/pinc_gkw

Abstract

High-fidelity scientific simulations are now producing unprecedented amounts of data, creating a storage and analysis bottleneck. A single simulation can generate tremendous data volumes, often forcing researchers to discard valuable information. A prime example of this is plasma turbulence described by the gyrokinetic equations: nonlinear, multiscale, and 5D in phase space. It constitutes one of the most computationally demanding frontiers of modern science, with runs taking weeks and yielding tens of terabytes of data dumps. The increasing storage demands underscore the importance of compression. However, reconstructed snapshots do not necessarily preserve essential physical quantities. We present a spatiotemporal evaluation pipeline, accounting for structural phenomena and multi-scale transient fluctuations to assess the degree of physical fidelity. Indeed, we find that various compression techniques lack preservation of both spatial mode structure and temporal turbulence characteristics. Therefore, we explore Physics-Informed Neural Compression (PINC), which incorporates physics-informed losses tailored to gyrokinetics and enables extreme compressions ratios of over $70,000\times$. Entropy coding on top of PINC further pushes it to $120,000\times$. This direction provides a viable and scalable solution to the prohibitive storage demands of gyrokinetics, enabling post-hoc analyses that were previously infeasible.

Keywords: Neural Compression, Physics-Informed Neural Networks, Plasma Physics, Gyrokinetics, Turbulence, Neural Fields, Vector Quantized Autoencoder

¹Institute for Machine Learning, JKU Linz ²United Kingdom Atomic Energy Authority, Culham campus ³EMMI AI GmbH, Linz. Correspondence to: Gianluca Galletti <g.galletti@ml.jku.at>.

Preprint. February 6, 2026.

1. Introduction

Scientific computing is on the cusp of entering an era of high-fidelity simulations across various domains, such as plasma physics (Fedeli et al., 2022; Chang et al., 2024; Dominski et al., 2024; Kelling et al., 2025; Siena et al., 2025), weather and climate modelling (Govett et al., 2024; Bodnar et al., 2024), astrophysics (Grete et al., 2025), and beyond. This progress is driven by advancements in High-Performance Computing (HPC): hardware accelerators, exascale computing systems, and scalable numerical solvers are pushing the horizon of what can be computed. These developments allow practitioners to move beyond reduced numerical approaches and attempt high-fidelity simulations, which are essential to accurately capture the underlying physics of complex systems. A striking instance of such simulations is gyrokinetics (Frieman & Chen, 1982; Krommes, 2012; Peeters et al., 2009), a five-dimensional (5D) nonlinear system that simulates turbulence in magnetised plasmas, such as those found in magnetically-confined fusion devices.

Gyrokinetic simulations generate massive data volumes that create a severe storage and analysis bottleneck. This arises from their 5D nature, combined with the high-resolution needed to model plasma turbulence. The gyrokinetic equations express the time evolution of particles in a plasma via a 5D distribution function $f \in \mathbb{C}^{v_{\parallel} \times \mu \times s \times x \times y}$, with spatial coordinates x, y, s and velocity-space coordinates v_{\parallel}, μ . A single run can produce tens of terabytes of data with snapshots saved at many time steps. In practice, researchers only store diagnostics, making comprehensive post-hoc analysis impossible. Compression offers a remedy by reducing the cost of storing full 5D fields. However, no evaluation framework currently exists to assess whether compressed snapshots preserve transient turbulence dynamics, an essential requirement for post-hoc analysis.

As a solution, we introduce an evaluation framework for transient turbulence characteristics in compressed snapshots of gyrokinetic simulations, disentangling *transient fluctuations*, which capture energy transfer across time, from *spatial* quantities that characterize a single snapshot. Various compression techniques fail to preserve spatial properties, as well as transient turbulence. To this end, we explore PINC for turbulent gyrokinetic data. We consider two paradigms:

autoencoders (e.g., VQ-VAE (van den Oord et al., 2017)) generalizing on unseen samples, and neural implicit representations (Park et al., 2019), which typically encode individual snapshots into network parameters. Unlike conventional compression, PINC enforces the preservation of key physical quantities, ensuring that downstream scientific analyses remain valid even at extreme compression rates.

We demonstrate that PINC achieves extreme storage reduction while preserving transient turbulence and steady-state spatial characteristics. Both autoencoders and neural fields attain reconstruction errors comparable to or better than conventional approaches at the same compression rate, while significantly improving physics preservation. A systematic rate-distortion scaling is also observed between compression rate, signal reconstruction and physics fidelity, allowing this trade-off to be estimated a priori. Lastly, we showcase additional weight space experiments such as latent temporal interpolation and hybrid compression (Section 4.3).

We summarize our contributions as follows. ① A spatiotemporal evaluation pipeline to assess physics preservation. It accounts for both spatial information and temporal dynamics, together capturing multi-scale transient fluctuations prevalent in turbulent dynamic. ② Physics-Informed, *Gyrokinetics-specific* training curricula for neural compression, PINC in short, equipping different techniques with physics losses capturing essential spatial integrals and turbulence characteristics. ③ As a benchmark for future works in (neural) compression, we publish a 50GB gyrokinetics validation set¹, paired with baseline results.

2. Related Work

Compression of spatiotemporal data is not a novel topic, and fields such as numerics and HPC conducted a plethora of research in this direction (Diffenderfer et al., 2019; Lakshminarasimhan et al., 2011; Lindstrom, 2014; Ballester-Ripoll et al., 2019; Momenifar et al., 2022). Related research exists in the domain of computational plasma physics (Anirudh et al., 2023), in particular for Particle-In-Cell (PIC) simulations (Birdsall & Langdon, 2005; Tskhakaya, 2008). The most relevant works include ISABELA (Lakshminarasimhan et al., 2011), an advanced spline method that promises almost lossless compression of spatiotemporal data of up to 7×; and VAPOR (Choi et al., 2021), a deep learning method based on autoencoders that compresses 2D PIC velocity space slices, supervised with mass, energy and momentum conservation losses. Concurrent work Kelling et al. (2025) proposes streaming pipelines for petascale PIC simulations, learning from data *in-transit* without intermediate storage. While PIC resolves the full 6D plasma kinetics, gyrokinetics reduces the problem to 5D by averaging over

fast gyromotion, enabling turbulent simulations too complex for PIC. Beyond compression methods, a closely related line of work is super-resolution, which seeks to reconstruct high-resolution fields from coarse inputs (Fukami et al., 2023; Yang et al., 2025; Page, 2025). We address the complementary challenge of compactly storing full snapshots.

Implicit Neural Fields encode information in a compact feature space, enabling scalable, grid-agnostic representation of high-resolution data. They represent continuous signals as coordinate-based learnable functions (Mildenhall et al., 2020; Park et al., 2019; Dupont et al., 2022a; Mescheder et al., 2019). In general, neural fields map input coordinates to the respective values of a field, i.e. $f_\theta : \mathbb{R}^d \rightarrow \mathbb{R}^n$ (Xie et al., 2021). They are usually implemented as MLPs with special activation functions (Sitzmann et al., 2020; Saragadam et al., 2023; Elfwing et al., 2017). In physics, neural fields have been applied to time-varying volumetric data compression (Han et al., 2024) and spatio-temporal dynamics forecasting using implicit frameworks (Serrano et al., 2023), among others.

Physics-Informed Neural Networks (PINNs) combine neural networks with physical constraints (Karniadakis et al., 2021). This is typically done by including additional loss terms (Raissi et al., 2019; Cai et al., 2021), ensuring that the laws of physics are obeyed. Constraints such as boundary conditions and conservation laws (Baez et al., 2024) are respected in the learned solutions, and more generally that neural network outputs remain consistent with the underlying differential equations. They have been especially effective in solving forward and inverse partial differential equation problems (Raissi et al., 2019). Inversely to the typical local, residual PINN losses, in our case they are global non-linear integrals which depend on the Fourier mode structure. Sitting at the intersection of PINNs and neural compression, Cranganore et al. (2025) combine neural fields with Sobolev training (Son et al., 2021; Czarnecki et al., 2017) to achieve impressive compression, tensor derivative accuracy and high-fidelity reconstruction on storage intensive general relativity data. Another notable mention is Momenifar et al. (2022), which uses a physics-informed VQ-VAE to capture velocity gradients and statistical properties in isoentropic flows. Our work systematically evaluates whether compressed representations accurately preserve plasma turbulence-specific quantities, motivating the need for specific physics-informed loss terms.

3. Method

3.1. Evaluating Plasma Turbulence

We assess whether compressed representations faithfully capture gyrokinetic turbulence through two complementary groups of metrics, focusing on: (1) spatial information, eval-

¹ gerkone/pinc_gkw on HuggingFace.

uated using non-linear field integrals and turbulence spectra, which measure how well the compressed representations preserve spatial mode structures and energy distributions. (2) Temporal consistency, via optimal transport of the transitional diagnostics and optical flow distance. These quantify the fidelity of the energy cascade and coherence of the reconstructed sequence.

Integrals. In gyrokinetics, (scalar) heat flux $Q \in \mathbb{R}$ and real-space electrostatic potential $\phi \in \mathbb{C}^{x \times s \times y}$ are two core quantities. They describe essential spatial and physical attributes of the density f . Q and ϕ are integrals of the distribution function f and are formulated as

$$\begin{aligned}\phi &= \mathbf{A} \int \mathbf{J}_0 f \, dv_{\parallel} d\mu, \\ Q &= \int \mathbf{B} \int \mathbf{v}^2 \phi f \, dv_{\parallel} d\mu \, dx dy ds.\end{aligned}\quad (1)$$

$\mathbf{A}, \mathbf{B} \in \mathbb{R}^{x \times s \times y}$ encompass geometric and physical parameters, $\mathbf{v} \in \mathbb{R}^{v_{\parallel} \times \mu}$ is the particle energy, and \mathbf{J}_0 denotes the 0th-order Bessel. The electrostatic potential ϕ is obtained by integrating the velocity-space of f , while the heat flux Q depends on both f and ϕ . Intuitively, ϕ represents spatial variations of the electric field, while Q is the energy flow carried by particles along field lines.

Wavespace distribution (diagnostics). These derived quantities are used by researchers to determine the properties of a simulation and to diagnose the soundness of a given configuration; they measure how energy and electrostatic fluctuations are distributed across modes in wavenumber space, and provide a basis for identifying behaviors and patterns in turbulent plasma transport. In particular, $k_y^{\text{spec}} \in \mathbb{C}^{N_{k_y}}$ describes the perpendicular scales of turbulence along y , and $Q^{\text{spec}} \in \mathbb{C}^{N_{k_y}}$ links turbulent structures to heat transport. They are expressed as convolutions of ϕ and Q ,

$$\begin{aligned}k_y^{\text{spec}}(y) &= \sum_{s,x} |\hat{\phi}(x, s, y)|^2, \\ Q^{\text{spec}}(y) &= \sum_{v_{\parallel}, \mu, s, x} \mathbf{Q}(v_{\parallel}, \mu, s, x, y),\end{aligned}\quad (2)$$

where $\hat{\phi}$ is the Fourier space electrostatic potential, and \mathbf{Q} is the heat flux field (also in Fourier space) before applying the outermost integral, which aggregates it to Q . Diagnostics are used to characterize turbulence, and can be analyzed both in a time-averaged or transient manner. Time dependency is used to observe how the energy cascade shifts in the energy to lower modes and vice versa, while statistically-steady forms (time-averaged, \bar{k}_y^{spec} and \bar{Q}^{spec})

define dominant modes. Namely, \bar{k}_y^{spec} is the mean turbulent spectrum, and \bar{Q}^{spec} quantifies the heat flux contribution to turbulent transport. They are both used by researchers to detect whether turbulence develops and at which scale.

Time dynamics. Turbulence is inherently a spatiotemporal phenomena, and a purely spatial evaluation is insufficient to assess reliable reconstruction. To that end, we include metrics from two different perspectives to quantify temporal consistency. First, the fidelity at which the onset of turbulence is reproduced can be assessed in the transitional phase, between the linear and the statistically-steady state. We quantitatively evaluate the time-accumulated optimal transport of the wavespace distributions k_y^{spec} and Q^{spec} (Equation (2)) through Wasserstein Distance (WD), and denote it as Energy Cascade (EC) error. It captures how well the bi-directional energy cascade is captured. Given two diagnostics sequences of N timesteps in the transition phase, $k_y^{\text{spec}}, Q^{\text{spec}}$ and predicted $\hat{k}_y^{\text{spec}}, \hat{Q}^{\text{spec}}$,

$$\begin{aligned}\text{EC}_{k_y} &= \sum_{i=1}^N \text{WD}(k_{y,i}^{\text{spec}}, \hat{k}_{y,i}^{\text{spec}}), \\ \text{EC}_Q &= \sum_{i=1}^N \text{WD}(Q_i^{\text{spec}}, \hat{Q}_i^{\text{spec}}).\end{aligned}\quad (3)$$

Second, to check the dynamic consistency of the decompressed sequence we employ the *EndPoint Error* (EPE) of the optical flow field (Baker et al., 2011), commonly used in video modeling (Argaw & Kweon, 2022; Ma et al., 2024). Additional definition in Section C.1. Given two sequences of x_1 and x_2 of N frames and their i -th flow vectors $\mathbf{F}_1^{(i)}$ and $\mathbf{F}_2^{(i)}$, the EndPoint Error is

$$\text{EPE}(x_1, x_2) = \frac{1}{N} \sum_{i=1}^N \|\mathbf{F}_1^{(i)} - \mathbf{F}_2^{(i)}\|_2. \quad (4)$$

3.2. Neural Compression

We identify two dominant approaches to learned compression, depending on a few key aspects. The first approach are autoencoders, with explicit latent space compression at the bottleneck between an encoder and a decoder. Parameters θ are shared across snapshots and time, and a single model Γ_{θ} is trained on a dataset. Compression is applied to unseen samples. VQ-VAE (van den Oord et al., 2017) exemplifies autoencoders designed for compression. In contrast, neural implicit representations overfit an independent set of parameters at each datapoint, for instance across time $[\Gamma_{\theta_t}]_{(0 \dots T)}$. Encoding is implicit in weight-space and reconstruction happens by querying the neural field. Figure 1 outlines PINC training and evaluation for a trajectory. The complex Mean Squared Error (cMSE) on the density f is

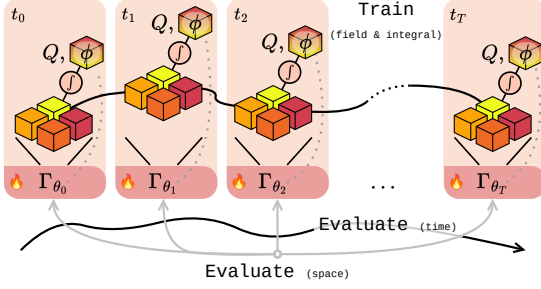


Figure 1. Sketch of the training and evaluation for Physics-Informed Neural Compression (PIN) models. Training is done at individual time snapshots, while evaluation considers turbulence taking both spatial and temporal information into account.

used as reconstruction loss in training

$$\mathcal{L}_{\text{recon}} = \sum_{v_{\parallel}, \mu, x, s, y} [\Re(f_{\text{pred}} - f_{\text{GT}})^2 + \Im(f_{\text{pred}} - f_{\text{GT}})^2]. \quad (5)$$

5D autoencoders. Due to the high-dimensional nature of the data, we leverage nD swin layers (Galletti et al., 2025; Paischer et al., 2025a), based on Shifted Window Attention (Liu et al., 2021), which promise scaling to higher dimensions. They work by first partitioning the domain in non-overlapping *windows*, then performing attention only locally within the window. An autoencoder $\Gamma_{\theta} : \mathbb{C}(v_{\parallel}, \mu, s, x, y) \times \mathbb{R}^4 \rightarrow \mathbb{C}^{v_{\parallel}, \mu, s, x, y}$, with $\Gamma_{\theta}(f, c) = \mathcal{D} \circ \mathcal{E}(f, c)$, encodes the 5D density field f and conditioning c containing four gyrokinetic parameters (R/L_T , R/L_n , q , and \hat{s}) into a compact latent space, then decodes it to reconstruct f . Following hierarchical vision transformers, the encoder \mathcal{E} tiles f into patches and applies interleaved Swin and downsampling layers. At the bottleneck, the latent dimension is downprojected to control the compression rate. The decoder \mathcal{D} mirrors this, with upsampling to restore the original resolution. We apply both regular Autoencoders (AE) and Vector-Quantized Variational Autoencoders (VQ-VAEs) (van den Oord et al., 2017). Autoencoders are *monolithic models* that compress in an explicit latent space, enabling cheap compression and decompression. However, they usually require expensive pretraining and a diverse dataset to generalize across different simulations.

Neural implicit fields. The distribution function f is indexed by a five-tuple of coordinates $(v_{\parallel}, \mu, s, x, y)$. Specifically, we train a separate (discrete) coordinate-based Neural Field $\Gamma_{\theta_{t,c}} : \mathbb{N}^5 \rightarrow \mathbb{C}$ to fit each f_t^c at time t of a trajectory configured by c . Indices are encoded with a learnable embedding hashmap (Müller et al., 2022), then passed to an MLP using SiLU (Elfwing et al., 2017), sine (Sitzmann et al., 2020) or Gabor (Saragadam et al., 2023) activations. Fitting a $\Gamma_{\theta_{t,c}}$ takes $\sim 1\text{-}2$ minutes (NVIDIA H100). Since independent networks are used per snapshot, training is fully

parallelized and performed in a staggered / pipelined fashion. Neural fields are *micromodels*: individual samples are implicitly encoded into network weights, offering resolution invariance and lower training requirements. Conversely, encoding is relatively costly.

3.3. Physics-Informed Neural Compression (PIN)

Training on $\mathcal{L}_{\text{recon}}$ alone cannot ensure conservation of physical quantities or turbulent characteristics. Further, due to the limited representation power, lossy compression inevitably discards useful information if left unconstrained. We supervise on the physical quantities listed in Section 3.1 by penalizing (absolute) deviations from the ground truth. Integral and wavespace losses are defined as

$$\begin{aligned} \mathcal{L}_Q &= |Q_{\text{pred}} - Q_{\text{GT}}|, & \mathcal{L}_{\phi} &= \text{L1}(\phi_{\text{pred}}, \phi_{\text{GT}}), \\ \mathcal{L}_{k_y^{\text{spec}}} &= \text{L1}(k_y^{\text{spec}, \text{pred}}, k_y^{\text{spec}, \text{GT}}), & \mathcal{L}_{Q^{\text{spec}}} &= \text{L1}(Q_{\text{pred}}^{\text{spec}}, Q_{\text{GT}}^{\text{spec}}). \end{aligned} \quad (6)$$

In addition, we introduce a first-order constraint to capture the turbulent energy cascade. In the case of simulations with a single energy injection scale, the spectra must be monotonically decreasing after the dominant mode, indexed by the peak wavenumber k_{peak} . This specific monotonicity loss can be written as the log-transformed isotonic loss, penalizing negative slopes,

$$\mathcal{L}_{\text{iso}}(\mathbf{s}) = \frac{1}{N - k_{\text{peak}}} \sum_{i=k_{\text{peak}}}^{N-1} \left| \ln[\mathbf{s}(i)] - \ln[\mathbf{s}(i)^{\text{sorted}}] \right|. \quad (7)$$

With $\mathbf{s} \in \mathbb{C}^N$ the diagnostic vector (k_y^{spec} and Q^{spec}). Combining all terms yields the final physics-informed loss:

$$\begin{aligned} \mathcal{L}_{\text{PIN}} &= \left. \mathcal{L}_Q + \mathcal{L}_{\phi} \right\}_{\mathcal{L}_{\text{int}}} + \\ &\quad \left. \mathcal{L}_{k_y^{\text{spec}}} + \mathcal{L}_{Q^{\text{spec}}} \right\}_{\mathcal{L}_{\text{diag}}} + \\ &\quad \left. \mathcal{L}_{\text{iso}}(k_y^{\text{spec}, \text{pred}}) + \mathcal{L}_{\text{iso}}(Q_{\text{pred}}^{\text{spec}}) \right\}_{\mathcal{L}_{\text{grad}}}. \end{aligned} \quad (8)$$

Importantly, our training supervises the model on nonlinear integrals of the distribution function, rather than directly on PDE residuals (Karniadakis et al., 2021) or derivatives (Son et al., 2021). PINC implicitly directs the network to the physically relevant modes. In turn, as Q and ϕ integrals depend on the full spectral structure of f , many of the losses in Equation (8) are *global* quantities, rather than the local pointwise supervision typical in PINNs. \mathcal{L}_{PIN} can be included in training, but with two caveats: (i) loss terms depend on f 's mode composition, and (ii) global loss terms cannot be computed at coordinate-level. We address (i) by applying \mathcal{L}_{PIN} after f 's have converged, to ensure that structure is present. (ii) is problematic only for local or sparse methods. The following sections detail the devices enabling PINC training on neural fields and autoencoders.

PINC-neural fields. Neural fields fit $\mathcal{L}_{\text{PINC}}$, continuing optimization after the initial steps where \mathbf{f} is learned. For stability, multi-objective optimizers offer a more principled alternative to manual tweaking or schedulers. Conflict-Free Inverse Gradients (Liu et al., 2024, ConFIG) and Augmented Lagrangian Multipliers (Basir & Senocak, 2023) are sometimes employed in tasks with many competing losses (Berzins et al., 2025). Finally, even though neural fields are normally trained on small sparse coordinate batches, $\mathcal{L}_{\text{PINC}}$ gradients can only be computed on the entire grid.

PINC-autoencoders. Training autoencoders with physics constraints across heterogeneous samples tends to result in training instabilities. To mitigate this, we employ parameter-efficient finetuning. Specifically, we pre-train the autoencoder on $\mathcal{L}_{\text{recon}}$, and finetune it on $\mathcal{L}_{\text{PINC}}$ using Explained Variance Adaptation (Paischer et al., 2025b, EVA), an improved and more stable variant of LoRA-style adapters (Hu et al., 2022). More training details in Section C.4.

4. Results

Neural fields are simple MLPs with SiLU activations (Elfwing et al., 2017), 64 latent dimension, 5 layers and skip connections. They are fit using AdamW (Loshchilov & Hutter, 2019) with learning rate decaying between $[5e-3, 1e-12]$ (details in Section C.5). Results suggest that neural fields trained with ConFIG are less accurate on physical losses, but lead to a marginally better reconstruction error (Appendix Table 8). For simplicity, all models reported are trained without loss balancing, unless specified otherwise. Grid searches and ablations are in Section C.5.

As for standard autoencoders and VQ-VAEs, swin tokens are 1024-dimensional, bottleneck dimension is 32, and the codebook dimension of the VQ-VAE is 128, totaling at $\sim 152\text{M}$ parameters. Both are trained and fine-tuned on 6,890 \mathbf{f} time snapshots, amounting to around 500GB of data (details in Section B). Compression and reconstruction is subse-

quently expected to happen *out of distribution*, to unseen trajectories. Pre-training takes ~ 60 hours (200 epochs, $4 \times$ NVIDIA H100) for standard AE and VQ-VAE. Fine-tuning with EVA weights takes ~ 28 hours on one NVIDIA H100 for 120 epochs, adapting $\sim 4\%$ (6M) of the total parameters. Optimized using Muon (Jordan et al., 2024) with cosine scheduling of the learning rate between $[2e-4, 4e-6]$ (details in Section C.4).

We compare with traditional compression based on different techniques: ZFP (Lindstrom, 2014), a very popular compression method for scientific data relying on block-quantization, Wavelet-based compression, spatial PCA and JPEG2000 adapted for the 5D data. Baselines are tuned to achieve compression rates (CRs) of around $1,000 \times$ (99.9% size reduction), comparable with neural fields and vanilla autoencoders. For reference, *off-the-shelf* traditional techniques such as `gzip` achieve a lossless compression ratio of $\sim 1.1x$ (8% reduction). Information on baselines can be found in Section C.2. Detailed information about runtime can be found in the Appendix Table 14.

4.1. Compression

Table 1 quantitatively summarizes the compression and reconstruction results. We evaluate all methods on traditional compression metrics, integral, and turbulence errors. To measure spatial \mathbf{f} reconstruction quality after compression, Peak Signal-to-Noise-Ratio (PSNR) is reported (defined in Section C.1). To evaluate temporal compression, we report the EndPoint Error (EPE) (Equation (4)) for turbulent snapshots of \mathbf{f} . Integral errors are reported as mean absolute error of flux Q and potential ϕ after integration of \mathbf{f} according to Equation (1). For steady-state turbulence evaluation we normalize the *time-averaged*, \bar{k}_y^{spec} and \bar{Q}^{spec} spectra and employ Wasserstein Distance (WD), which is commonly used as a geometry-aware distance metric and can efficiently be computed for 1D spectra. We report additional metrics for spatial evaluation in Table 13. Furthermore, for discussion on transient dynamics see Paragraph 4.2 (Figure 4).

Table 1. Comparison between PINC and traditional methods. Evaluation on 420 total \mathbf{f}_t^c s (20 turbulent trajectories, 21 timesteps), sampled in the statistically steady phase. Errors in data space. Best result in bold, second best underlined.

		Compression \mathbf{f}		Integrals Q, ϕ		Turbulence $Q^{\text{spec}}, k_y^{\text{spec}}$	
	CR	PSNR \uparrow	EPE \downarrow	L1(Q) \downarrow	PSNR(ϕ) \uparrow	WD(\bar{k}_y^{spec}) \downarrow	WD(\bar{Q}^{spec}) \downarrow
ZFP	$901 \times$	28.97 ± 1.09	0.175 ± 0.07	107.48 ± 49.35	-16.20 ± 7.09	0.020 ± 0.01	0.116 ± 0.20
Wavelet	$936 \times$	33.07 ± 1.18	0.064 ± 0.03	107.74 ± 49.51	-13.24 ± 9.20	0.020 ± 0.01	$\mathbf{0.010} \pm 0.00$
PCA	$1020 \times$	32.09 ± 0.98	0.123 ± 0.07	67.60 ± 36.08	-10.22 ± 6.89	0.020 ± 0.01	0.011 ± 0.00
JPEG2000	$1000 \times$	34.33 ± 0.95	0.046 ± 0.02	103.91 ± 44.12	-20.85 ± 6.50	0.020 ± 0.01	0.035 ± 0.03
NF	$1167 \times$	36.91 ± 0.93	0.031 ± 0.02	61.50 ± 16.91	1.24 ± 5.99	0.017 ± 0.01	0.017 ± 0.00
PINC-NF	$1167 \times$	<u>35.76 ± 1.38</u>	<u>0.037 ± 0.02</u>	2.18 ± 8.33	13.50 ± 4.44	0.006 ± 0.00	0.015 ± 0.00
AE + EVA	$716 \times$	<u>35.64 ± 2.03</u>	<u>0.063 ± 0.05</u>	<u>15.01 ± 16.42</u>	6.72 ± 4.98	0.016 ± 0.01	0.012 ± 0.01
VQ-VAE + EVA	$77368 \times$	32.61 ± 1.58	0.095 ± 0.07	<u>44.26 ± 40.97</u>	<u>7.66 ± 3.75</u>	<u>0.015 ± 0.01</u>	0.013 ± 0.01

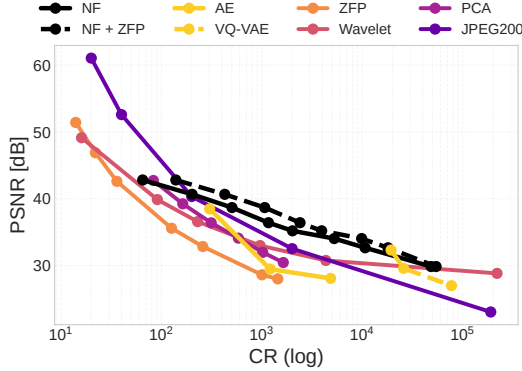


Figure 2. Compression performance rate-distortion as Peak Signal to Noise Ratio (PSNR) on Compression Rate (CR) on 3 randomly sampled timesteps from 10 trajectories (30 total samples).

Qualitative examples of reconstructions for f and ϕ are in the Appendix at Figures 11 and 12.

At similar compression, non-PINC neural fields and autoencoders improve upon traditional methods on quality, as well as integrated quantities and turbulence. However, especially integral metrics ($L_1(Q)$ and $PSNR(\phi)$) exhibit excessive discrepancies from the ground-truth. This motivates PINC soft-constraints on the optimization to preserve them.

Comparing NF to PINC-NF reveals improvements on integral errors at a minor reconstruction degradation. Furthermore, WD decreases by almost $3\times$ for \bar{k}_y^{spec} . Interestingly, we do not observe an improvement on Q^{spec} , possibly due to competing objectives. A possible interpretation for these two patterns is that, since modeling capacity is constrained by high compression, the available ‘‘entropy’’ gets allocated across modes, according to the encoding algorithm. In neural networks, the spectral bias (Rahaman et al., 2019) of MSE training (Equation (5)) implies that high-energy components have priority during training, while lower modes converge slower. PINC appears to redistribute some of the energy to more physically relevant modes. For example, the heat flux integral masks low frequencies and rescales high frequencies, giving them more importance.

Performance-rate scaling. To assess how reconstruction quality scales across compression levels, we train a series of neural fields and autoencoders with progressively larger parameter counts and latent sizes. Training neural fields remains relatively inexpensive, whereas autoencoders become unfeasible in terms of both GPU memory and runtime at lower CRs. Consequently, we train only six autoencoders in total (three standard and three VQ-VAEs), all at comparatively high CRs ($>1,000\times$). Findings reported in Figure 2 suggest that both learned methods present a specific ‘‘window’’ of CRs in which they significantly outperform traditional baselines (namely in the $500 - 10,000\times$

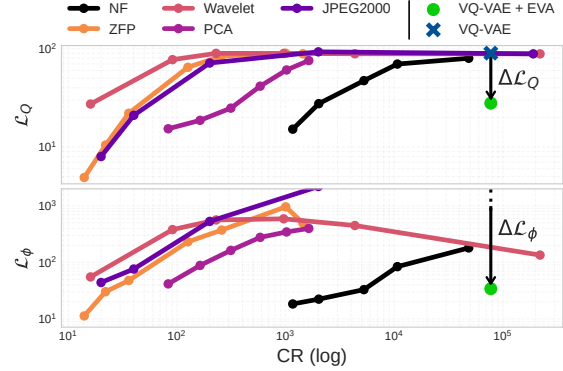


Figure 3. Physical loss scaling as \mathcal{L}_Q (top) and \mathcal{L}_ϕ (bottom) on Compression Rate (log-log). NF and VQ-VAE + EVA are trained with PINC losses. Arrow denotes $\Delta\mathcal{L}$ improvement for VQ-VAE.

range). Moreover, neural fields also exhibit a favorable exponential decay (linearly in semilog-x), as opposed to super-exponential of others (polynomial in semilog-x). This is supported by neural field compression on other modalities (Dupont et al., 2022b; Bauer et al., 2023). In terms of reconstruction quality, at lower rates ($< 200\times$) neural compression cannot reliably match wavelets or JPEG2000, and at extreme CRs ($> 40,000\times$) they are comparable.

4.2. Physics and Turbulence Preservation

Physical scaling. Similarly to Figure 2 for rate-distortion for f , Figure 3 shows scaling for heat flux Q and electrostatic potential ϕ integral losses as CR is changed. Figure 12 shows corresponding projections of the 3D ϕ integral and residuals ($CR = \sim 1,000\times$). Traditional compression struggles to capture ϕ even at low CR, while PINC models trained on Equation (8) as well as the reconstruction loss (Equation (5)) yield reasonable reconstruction.

Recovering turbulence. Figure 4 qualitatively shows how well different models capture the direct energy cascade

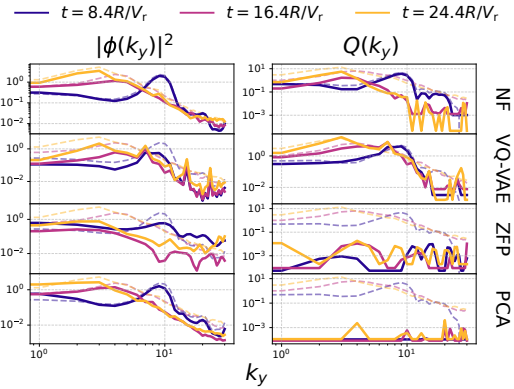


Figure 4. Energy cascade visualized as the transfer from higher to lower modes as turbulence develops. Plots in loglog scale.

Table 2. Temporal consistency: endpoint error (EPE) and energy cascade Wasserstein (EC). Evaluation on 270 f_t^c s (30 trajectories, 9 timesteps) from the transition phase where mode growth happens.

Model	EPE \downarrow	EC $_{k_y}$ \downarrow	EC $_Q$ \downarrow
ZFP	0.058 ± 0.03	0.031 ± 0.01	0.715 ± 1.30
Wavelet	0.033 ± 0.01	0.031 ± 0.01	0.061 ± 0.09
PCA	0.032 ± 0.02	0.032 ± 0.01	0.065 ± 0.07
JPEG2000	0.027 ± 0.01	0.032 ± 0.01	0.176 ± 0.21
NF	0.017 ± 0.01	0.030 ± 0.01	0.029 ± 0.02
PINC-NF	0.030 ± 0.02	0.011 ± 0.01	0.015 ± 0.00
PINC-AE	0.030 ± 0.02	0.028 ± 0.01	0.005 ± 0.00
PINC-VQ-VAE	0.036 ± 0.02	0.018 ± 0.01	0.008 ± 0.00

phenomena across different simulations (energy shifting to lower modes over time), by visualizing the *per-timestep* spectra k_y^{spec} and Q^{spec} in a log-log plot. The Figure provides a qualitative comparison of turbulence recovery on the temporal axis, in contrast to the time-averaged statistics reported in Table 1. The time snapshots examined in Figure 4 (sampled between $[8.4, 24.4]R/V_r$ with a step size of $\Delta = 2.0R/V_r$) are sampled in the transitional phase where turbulence grows, at the so called *overshoot*. These timesteps are different to those in Table 1. On k_y^{spec} , traditional compression methods already achieve reasonable performance in most cases, but on Q^{spec} they produce severely nonphysical results (flat curves, negative numbers). Another observation is that, even though non-ML methods have fairly low Wasserstein distance in Table 1, this is not reflected at the overshoot. In contrast, neural fields and VQ-VAE can reproduce the overall profiles consistently, with VQ-VAE excelling at the flux spectra. However, both often fail to capture the higher-frequency magnitudes. The behaviors can be attributed to the spectral bias of neural networks (Rahaman et al., 2019; Teney et al., 2025), where low-frequency (high-energy) components are favored over high-frequencies. Section C.6 shows additional cascade plots for all methods and trajectories.

Table 2 shows that neural compression can significantly outperform traditional methods both on energy cascade errors (Equation (3)), as well as the endpoint error of f ’s optical flow (Equation (4)). We observe that PINC-NFs get less aligned over time, as reflected by the higher EPE and motivated to the performance drop discussed in Section 4.1. Conversely, they significantly outperform unregularized NFs on the two energy cascade metrics, suggesting a better representation of turbulence. Note that the EPE reported here differs from the one in Table 1: here it is applied to the transition phase, instead of the statistically steady one.

Physical losses ablations. We verify the impact of each loss term described in Equation (8) by training different models on each term in Section 3.1 and Section 3.3 separately,

Table 3. PINC losses ablations from Equation (8) (color-coded blocks). * means $> 100 \times$ larger than column average.

Model	Loss	PSNR(f)	\mathcal{L}_Q	\mathcal{L}_ϕ	$\mathcal{L}_{k_y^{\text{spec}}}$	$\mathcal{L}_{Q^{\text{spec}}}$
NF	$\mathcal{L}_{\text{recon}}$	38.89	48.59	4.45	3.71	1.52
	$+\mathcal{L}_{\text{int}}$	36.68	10.35	2.55	1.61	1.42
	$+\mathcal{L}_{\text{diag}}$	38.76	41.39	2.25	1.67	1.32
	$+\mathcal{L}_{\text{grad}}$	37.29	63.94	44.18	*	2.0
	$+\mathcal{L}_{\text{PINC}}$	38.28	28.03	1.41	0.24	1.41
VQ-VAE	$\mathcal{L}_{\text{recon}}$	26.96	86.21	*	*	91.68
	$+\mathcal{L}_{\text{PINC}}$	27.73	85.06	103.50	*	*
	$+\mathcal{L}_{\text{PINC}}$	32.21	27.73	40.81	284.96	59.84

for both autoencoders and neural fields. Table 3 collects the ablation findings. Training \mathcal{L}_{int} and $\mathcal{L}_{\text{diag}}$ have similar effects, both improve the integral as well as the diagnostics, with the integral being more informative. The model still gets valuable information on Q and ϕ from the gradients through $\mathcal{L}_{\text{diag}}$. In contrast, $\mathcal{L}_{\text{grad}}$ alone has a destabilizing effect, and is only effective when combined with other losses as it is dependent on how accurately the diagnostics (and integrals) are captured. Finally, the composite $\mathcal{L}_{\text{PINC}} = \mathcal{L}_{\text{int}} + \mathcal{L}_{\text{diag}} + \mathcal{L}_{\text{grad}}$ gathers benefits of each component.

Overall both classes of methods greatly improve performance on physical losses when trained on $\mathcal{L}_{\text{PINC}}$, while slightly decreasing f PSNR. The degradation in reconstruction observed for neural fields is connected to the interpretation of the physical loss scaling behaviors (Section 4.2): as minimizing $\mathcal{L}_{\text{PINC}}$ shifts the modes to ones relevant for integrals and diagnostics, some of the dominant ones of f become less represented and the decoded quality slightly degrades. While neural field training is generally consistent, for autoencoders severe instabilities emerge when training jointly on $\mathcal{L}_{\text{recon}} + \mathcal{L}_{\text{PINC}}$. Our EVA finetuning procedure is consistently outperforming and more stable than directly training on $\mathcal{L}_{\text{PINC}}$ (bottom of Table 3).

4.3. Representation Space Experiments

Table 4. Hybrid compression.

Metric	ZFP	ZipNN
Extra CR	$2.1 \times$	$1.2 \times$
Δ PSNR(f) \uparrow	-2c-4%	0%
Δ L1(Q) \downarrow	+8e-3%	0%
Δ L1(ϕ) \downarrow	+9.5%	0%

Table 5. Latent interpolation.

Model	PSNR
Extremes	16.7
f (data)	19.6
NF (weights)	18.9
VQ-VAE (latents)	20.5

Hybrid compression. Neural methods can further improve the compression rate when coupled with traditional techniques on the learned representations. Similarly to how data can be compressed into a low dimensional encoding, model parameters and autoencoder features are redundant and also lie on a lower-dimensional manifold. This is related to pruning (LeCun et al., 1990; Han et al., 2015), network

compression (Hershcovitch et al., 2024), and the lottery ticket hypothesis (Frankle & Carbin, 2019).

Improved compression can be achieved either with (lossless) entropy coding (Hershcovitch et al., 2024) or (lossy) quantization methods (Lindstrom, 2014). We apply both to neural fields and present findings in Table 4. ZipNN is lossless and does not induce any performance change, while providing a modest CR boost. ZFP is lossy with (tolerance of 10^{-3}), leading to some performance degradation and $2.1 \times$ CR. Both results are averaged on 60 random samples from 10 trajectories. We also show NF + ZFP in Figure 2. It closely follows the slope of NF but is right-shifted, achieving better CR. Notably, at the higher regimes they appear to converge suggesting diminishing returns. As an utmost example, we apply entropy coding on the VQ-VAE indices, raising the compression to $121492 \times$ (see Section C.4).

Latent (and weight space) interpolation. Representational consistency and compactness over different snapshots is a desired property of compression methods. It enables temporal coarsening (Ohana et al., 2024; Toshev et al., 2023) by interpolation in weight/latent space resulting in additional gains in CR as not every single snapshot needs to be compressed. To this end, we design an experiment to assess whether PINC models exhibit representational consistency across time. We encode two *extremes* f_a, f_b separated by ΔT and reconstruct intermediates f_t for $t = a, a + dT, \dots, b$ by linearly interpolating the representations (latents or weights) Z_{f_a} and Z_{f_b} .

For standard autoencoders, latent-space interpolation is a common practice (Berthelot* et al., 2019). In the case of VQ-VAEs, the latents are interpolated before quantization to produce more accurate reconstructions. It is not as straightforward for neural fields, as the parameters are not necessarily canonically ordered and exhibit various neuron symmetries (Hecht-Nielsen, 1990; Godfrey et al., 2022). To address this, we use a shared *meta neural field* trained on all extremes before finetuning it on each of them separately, improving weight alignment. This is similar to the initialization strategy used by Luigi et al. (2023) and Erkoç et al. (2023) to generate an aligned dataset of neural fields.

Table 5 provides compelling evidence that linearly interpolating in representation space improves over simply taking the extremes, and approximates linear interpolation in data space. It shows time coarsening by evaluating on middle snapshot $t_m = t_l + \frac{\Delta T}{2}$. Interpolating representations is comparable to data-space and has more information than the extremes. Results are averaged on 50 (unseen) midpoints on 10 trajectories, with $\Delta T = 8R/V_r$. Figure 10 illustrates intermediate reconstructions over time as progressive interpolation between Z_{f_a} and Z_{f_b} . However, because the underlying simulations are highly nonlinear accurate linear

interpolation is unlikely, hence the low reported PSNR. Regardless, we reckon that these results shows that learned representations are compact and self-consistent over time.

5. Conclusions

Our study provides compelling evidence that Physics-Informed Neural Compression (PINC) improves compression rate while maintaining underlying characteristics for gyrokinetic simulations of plasma turbulence. This is achieved by constraining training to maintain integral quantities and spectral shapes across key dimensions of the 5D fields. We anticipate that this approach can potentially be extended to other scientific domains, enabling practitioners to store compressed simulations that accurately capture specified physical phenomena across time and space, something previously infeasible due to storage requirements. These tools could considerably improve data accessibility and transfer, accelerating research across scientific communities.

The compression methods presented in this work could be combined with *neural operators*, nonlinearly evolving them in time. A major benefit of this is a significant reduction in dataset size required to train a surrogate model. Orthogonally, exploring physics-informed "functsets" (Dupont et al., 2022a; Jo et al., 2025) could be a valuable direction to further improve compression of neural fields for transient simulations and enable in-transit processing of data. Related approaches in this regard include continual learning (Yan et al., 2021; Woo et al., 2025), and in general ways to incorporate temporal dynamics into the training to enable on-the-fly (*in-situ*) compression of simulation snapshots.

Limitations. First, temporal information is not incorporated during PINC training, which we expect to especially improve on compression ratio and temporal consistency. Due to the computational complexity of training neural fields and especially autoencoders, this is left to future work. Second, the computational requirements are substantial, mirrored in the training times (Table 14). Even for neural fields, compression times are rather high and a consumer grade GPU is required. Finally, the proposed physics-informed losses are specific to gyrokinetics, limiting transferability to other scientific areas beyond plasma physics. Concurrent neural compression works, such as Momenifar et al. (2022) for fluid dynamics and Cranganore et al. (2025) for General Relativity, are also problem-specific. To our knowledge there is no general loss reformulation that is applicable to any problem, and we leave generalizing PINC to other domains as future work. We postulate that the strategies and methodologies used for gyrokinetics-PINC, for example the stabilization with EVA finetuning used for the autoencoders, can be successfully applied to other sources.

Impact Statement

The potential impact of our work extends beyond machine learning, and the main purpose is to facilitate scientific discovery in computational plasma physics and general numerics. It does not warrant further discussion on the ethics.

Reproducibility statement

Training and experiment code is submitted as a zip file in the supplementary materials. It contains autoencoders, neural fields and baseline implementation, as well as the configuration files used to obtain the paper results. The readme briefly outlines the code structure and describes how to start autoencoder/neural field training runs. Some further information on training is already present in the Method and Results sections, as well as dedicated sections in the Appendix. Unfortunately, the dataset used to train the autoencoders is not easily distributable due to its size. It was generated with the GKW (Peeters et al., 2009) flux tube gyrokinetic numerical solver, as detailed in Section B. A template for the configuration file used by GKW to start a run is included in the supplementary materials (data_generation/ directory). Parameter ranges used to generate the dataset are included both in the supplementary as well as in Section B for transparency. We release on huggingface a validation dataset along with neural field weights and autoencoder checkpoints [at this link](#). These samples allow to reproduce the main results displayed in Table 1.

References

Anirudh, R., Archibald, R., Asif, M. S., Becker, M. M., Benkadda, S., Bremer, P.-T., Budé, R. H. S., Chang, C. S., Chen, L., Churchill, R. M., Citrin, J., Gaffney, J. A., Gainaru, A., Gekelman, W., Gibbs, T., Hamaguchi, S., Hill, C., Humbird, K., Jalas, S., Kawaguchi, S., Kim, G.-H., Kirchen, M., Klasky, S., Kline, J. L., Krushelnick, K., Kustowski, B., Lapenta, G., Li, W., Ma, T., Mason, N. J., Mesbah, A., Michoski, C., Munson, T., Murakami, I., Najm, H. N., Olofsson, K. E. J., Park, S., Peterson, J. L., Probst, M., Pugmire, D., Sammuli, B., Sawlani, K., Scheinker, A., Schissel, D. P., Shalloo, R. J., Shinagawa, J., Seong, J., Spears, B. K., Tennyson, J., Thiagarajan, J., Ticoş, C. M., Trieschmann, J., Dijk, J. v., Essen, B. V., Ventzek, P., Wang, H., Wang, J. T. L., Wang, Z., Wende, K., Xu, X., Yamada, H., Yokoyama, T., and Zhang, X. 2022 review of data-driven plasma science. *IEEE Transactions on Plasma Science*, 51(7):1750–1838, July 2023. ISSN 1939-9375. doi: 10.1109/tps.2023.3268170.

Argaw, D. M. and Kweon, I.-S. Long-term video frame interpolation via feature propagation. *2022 IEEE/CVF Conference on Computer Vision and Pattern Recognition (CVPR)*, pp. 3533–3542, 2022.

Baez, A., Zhang, W., Ma, Z., Das, S., Nguyen, L. M., and Daniel, L. Guaranteeing conservation laws with projection in physics-informed neural networks, 2024.

Baker, S., Scharstein, D., Lewis, J. P., Roth, S., Black, M. J., and Szeliski, R. A database and evaluation methodology for optical flow. *Int. J. Comput. Vision*, 92(1):1–31, March 2011. ISSN 0920-5691. doi: 10.1007/s11263-010-0390-2.

Ballester-Ripoll, R., Lindstrom, P., and Pajarola, R. Tthresh: Tensor compression for multidimensional visual data. *IEEE Transaction on Visualization and Computer Graphics*, to appear, 2019. arXiv:1806.05952.

Basir, S. and Senocak, I. An adaptive augmented lagrangian method for training physics and equality constrained artificial neural networks, 2023.

Bauer, M., Dupont, E., Brock, A., Rosenbaum, D., Schwarz, J. R., and Kim, H. Spatial functa: Scaling functa to imangenet classification and generation. *arXiv preprint arXiv: 2302.03130*, 2023.

Berthelot*, D., Raffel*, C., Roy, A., and Goodfellow, I. Understanding and improving interpolation in autoencoders via an adversarial regularizer. In *International Conference on Learning Representations*, 2019.

Berzins, A., Radler, A., Volkmann, E., Sanokowski, S., Hochreiter, S., and Brandstetter, J. Geometry-informed neural networks, 2025.

Birdsall, C. K. and Langdon, A. B. *Plasma physics via computer simulation*. New York: Taylor and Francis, first edition, 2005.

Bodnar, C., Bruinsma, W. P., Lucic, A., Stanley, M., Brandstetter, J., Garvan, P., Riechert, M., Weyn, J. A., Dong, H., Vaughan, A., Gupta, J. K., Thambiratnam, K., Archibald, A., Heider, E., Welling, M., Turner, R. E., and Perdikaris, P. Aurora: A foundation model of the atmosphere. *CoRR*, abs/2405.13063, 2024. doi: 10.48550/ARXIV.2405.13063.

Cai, S., Mao, Z., Wang, Z., Yin, M., and Karniadakis, G. E. Physics-informed neural networks (pinns) for fluid mechanics: A review, 2021.

Chang, C., Ku, S., Hager, R., Choi, J., Pugmire, D., Klasky, S., Loarte, A., and Pitts, R. Role of turbulent separatrix tangle in the improvement of the integrated pedestal and heat exhaust issue for stationary-operation tokamak fusion reactors. *Nuclear Fusion*, 64(5):056041, apr 2024. doi: 10.1088/1741-4326/ad3b1e.

Chen, Z., Badrinarayanan, V., Lee, C.-Y., and Rabinovich, A. GradNorm: Gradient normalization for

adaptive loss balancing in deep multitask networks. In Dy, J. and Krause, A. (eds.), *Proceedings of the 35th International Conference on Machine Learning*, volume 80 of *Proceedings of Machine Learning Research*, pp. 794–803. PMLR, 10–15 Jul 2018.

Choi, J., Churchill, M., Gong, Q., Ku, S.-H., Lee, J., Rangarajan, A., Ranka, S., Pugmire, D., Chang, C., and Klasky, S. Neural data compression for physics plasma simulation. In *Neural Compression: From Information Theory to Applications – Workshop @ ICLR 2021*, 2021.

Christopoulos, C. A., Ebrahimi, T., and Skodras, A. N. Jpeg2000: the new still picture compression standard. In *Proceedings of the 2000 ACM Workshops on Multimedia, MULTIMEDIA '00*, pp. 45–49, New York, NY, USA, 2000. Association for Computing Machinery. ISBN 1581133111. doi: 10.1145/357744.357757.

Cranganore, S. S., Bodnar, A., Berzins, A., and Brandstetter, J. Einstein fields: A neural perspective to computational general relativity, 2025.

Czarnecki, W. M., Osindero, S., Jaderberg, M., Swirszcz, G., and Pascanu, R. Sobolev training for neural networks. In *Proceedings of the 31st International Conference on Neural Information Processing Systems, NIPS'17*, pp. 4281–4290, Red Hook, NY, USA, 2017. Curran Associates Inc. ISBN 9781510860964.

Diffenderfer, J., Fox, A. L., Hittinger, J. A., Sanders, G., and Lindstrom, P. G. Error analysis of zfp compression for floating-point data. *SIAM Journal on Scientific Computing*, 41(3):A1867–A1898, 2019.

Dominski, J., Chang, C. S., Hager, R., Ku, S., Yoon, E. S., and Parail, V. Neoclassical transport of tungsten ion bundles in total-f neoclassical gyrokinetic simulations of a whole-volume jet-like plasma. *Physics of Plasmas*, 31(3):032303, 03 2024. ISSN 1070-664X. doi: 10.1063/5.0144509.

Dupont, E., Kim, H., Eslami, S. M. A., Rezende, D., and Rosenbaum, D. From data to functa: Your data point is a function and you can treat it like one. *arXiv preprint arXiv:2201.12204*, 2022a. Preprint.

Dupont, E., Loya, H., Alizadeh, M., Goliński, A., Teh, Y. W., and Doucet, A. Coin++: Neural compression across modalities, 2022b.

Elfwing, S., Uchibe, E., and Doya, K. Sigmoid-weighted linear units for neural network function approximation in reinforcement learning, 2017.

Erkoç, Z., Ma, F., Shan, Q., Nießner, M., and Dai, A. Hyperdiffusion: Generating implicit neural fields with weight-space diffusion, 2023.

Fedeli, L., Huebl, A., Boillod-Cerneux, F., Clark, T., Gott, K., Hillairet, C., Jaure, S., Leblanc, A., Lehe, R., Myers, A., Piechurski, C., Sato, M., Zaim, N., Zhang, W., Vay, J.-L., and Vincenti, H. Pushing the frontier in the design of laser-based electron accelerators with groundbreaking mesh-refined particle-in-cell simulations on exascale-class supercomputers. In *SC22: International Conference for High Performance Computing, Networking, Storage and Analysis*, pp. 1–12, 2022. doi: 10.1109/SC41404.2022.00008.

Frankle, J. and Carbin, M. The lottery ticket hypothesis: Finding sparse, trainable neural networks, 2019.

Frieman, E. and Chen, L. Nonlinear gyrokinetic equations for low-frequency electromagnetic waves in general plasma equilibria. *The Physics of Fluids*, 25(3):502–508, 1982.

Fukami, K., Fukagata, K., and Taira, K. Super-resolution analysis via machine learning: a survey for fluid flows. *Theoretical and Computational Fluid Dynamics*, 37(4):421–444, June 2023. ISSN 1432-2250. doi: 10.1007/s00162-023-00663-0.

Fukushima, K. Visual feature extraction by a multi-layered network of analog threshold elements. *IEEE Transactions on Systems Science and Cybernetics*, 5(4):322–333, 1969. doi: 10.1109/TSSC.1969.300225.

Galletti, G., Paischer, F., Setinek, P., Hornsby, W., Zanisi, L., Carey, N., Pamela, S., and Brandstetter, J. 5d neural surrogates for nonlinear gyrokinetic simulations of plasma turbulence, 2025.

Godfrey, C., Brown, D., Emerson, T., and Kvinge, H. On the symmetries of deep learning models and their internal representations. In Koyejo, S., Mohamed, S., Agarwal, A., Belgrave, D., Cho, K., and Oh, A. (eds.), *Advances in Neural Information Processing Systems*, volume 35, pp. 11893–11905. Curran Associates, Inc., 2022.

Govett, M., Bah, B., Bauer, P., Berod, D., Bouchet, V., Corti, S., Davis, C., Duan, Y., Graham, T., Honda, Y., Hines, A., Jean, M., Ishida, J., Lawrence, B., Li, J., Luterbacher, J., Muroi, C., Rowe, K., Schultz, M., Visbeck, M., and Williams, K. Exascale computing and data handling: Challenges and opportunities for weather and climate prediction. *Bulletin of the American Meteorological Society*, 105(12):E2385 – E2404, 2024. doi: 10.1175/BAMS-D-23-0220.1.

Grete, P., O’Shea, B. W., Glines, F. W., Prasad, D., Wibking, B. D., Fournier, M., Brüggen, M., and Voit, M. The xmagnet exascale mhd simulations of smbh feedback in galaxy groups and clusters: Overview and preliminary cluster results, 2025.

Han, J., Zheng, H., and Bi, C. Kd-inr: Time-varying volumetric data compression via knowledge distillation-based implicit neural representation. *IEEE Transactions on Visualization and Computer Graphics*, 30(10):6826–6838, October 2024. ISSN 1077-2626. doi: 10.1109/TVCG.2023.3345373.

Han, S., Mao, H., and Dally, W. J. Deep compression: Compressing deep neural networks with pruning, trained quantization and huffman coding. *arXiv preprint arXiv:1510.00149*, 2015.

Hecht-Nielsen, R. On the algebraic structure of feed-forward network weight spaces. In ECKMILLER, R. (ed.), *Advanced Neural Computers*, pp. 129–135. North-Holland, Amsterdam, 1990. ISBN 978-0-444-88400-8. doi: <https://doi.org/10.1016/B978-0-444-88400-8.50019-4>.

Hendrycks, D. and Gimpel, K. Gaussian error linear units (gelus), 2023.

Hershcovitch, M., Wood, A., Choshen, L., Girmonsky, G., Leibovitz, R., Ennmouri, I., Malka, M., Chin, P., Sundararaman, S., and Harnik, D. Zipnn: Lossless compression for ai models. *arXiv preprint arXiv:2411.05239*, 2024.

Horn, B. K. and Schunck, B. G. Determining optical flow. *Artificial Intelligence*, 17(1):185–203, 1981. ISSN 0004-3702. doi: [https://doi.org/10.1016/0004-3702\(81\)90024-2](https://doi.org/10.1016/0004-3702(81)90024-2).

Hu, E. J., Shen, Y., Wallis, P., Allen-Zhu, Z., Li, Y., Wang, S., Wang, L., and Chen, W. Lora: Low-rank adaptation of large language models. In *ICLR*, 2022.

Huffman, D. A. A method for the construction of minimum-redundancy codes. *Proceedings of the IRE*, 40(9):1098–1101, 1952. doi: 10.1109/JRPROC.1952.273898.

Jo, M., Cho, W., Mudiyanselage, U. B., Lee, S., Park, N., and Lee, K. Pdefuncta: Spectrally-aware neural representation for pde solution modeling, 2025.

Jordan, K., Jin, Y., Boza, V., Jiacheng, Y., Cesista, F., Newhouse, L., and Bernstein, J. Muon: An optimizer for hidden layers in neural networks, 2024.

Karniadakis, G. E., Kevrekidis, I. G., Lu, L., Perdikaris, P., Wang, S., and Yang, L. Physics-informed machine learning. *Nature Reviews Physics*, 3(6):422–440, 2021. ISSN 2522-5820. doi: 10.1038/s42254-021-00314-5.

Kelling, J., Bolea, V., Bussmann, M., Checkervarty, A., Debus, A., Ebert, J., Eisenhauer, G., Gutta, V., Kesselheim, S., Klasky, S., Pandit, V., Pausch, R., Podhorszki, N., Poschel, F., Rogers, D., Rustamov, J., Schmerler, S., Schramm, U., Steiniger, K., Widera, R., Willmann, A., and Chandrasekaran, S. The artificial scientist – in-transit machine learning of plasma simulations, 2025.

Krommes, J. A. The gyrokinetic description of micro-turbulence in magnetized plasmas. *Annual Review of Fluid Mechanics*, 44(Volume 44, 2012):175–201, 2012. ISSN 1545-4479. doi: <https://doi.org/10.1146/annurev-fluid-120710-101223>.

Lakshminarasimhan, S., Shah, N., Ethier, S., Klasky, S., Latham, R., Ross, R., and Samatova, N. F. Compressing the incompressible with isabela: In-situ reduction of spatio-temporal data. In Jeannot, E., Namyst, R., and Roman, J. (eds.), *Euro-Par 2011 Parallel Processing*, pp. 366–379, Berlin, Heidelberg, 2011. Springer Berlin Heidelberg. ISBN 978-3-642-23400-2.

LeCun, Y., Denker, J. S., and Solla, S. A. Optimal brain damage. *Advances in neural information processing systems*, 2, 1990.

Li, Z., Kovachki, N., Azizzadenesheli, K., Liu, B., Bhattacharya, K., Stuart, A., and Anandkumar, A. Fourier neural operator for parametric partial differential equations, 2021.

Lindstrom, P. Fixed-rate compressed floating-point arrays. *IEEE Transactions on Visualization and Computer Graphics*, 20(12):2674–2683, 2014.

Liu, Q., Chu, M., and Thuerey, N. Config: Towards conflict-free training of physics informed neural networks. In *The Thirteenth International Conference on Learning Representations*, 2024.

Liu, Z., Lin, Y., Cao, Y., Hu, H., Wei, Y., Zhang, Z., Lin, S., and Guo, B. Swin transformer: Hierarchical vision transformer using shifted windows. In *2021 IEEE/CVF International Conference on Computer Vision, ICCV 2021, Montreal, QC, Canada, October 10-17, 2021*, pp. 9992–10002. IEEE, 2021. doi: 10.1109/ICCV48922.2021.00986.

Loshchilov, I. and Hutter, F. Decoupled weight decay regularization, 2019.

Luigi, L. D., Cardace, A., Spezialetti, R., Ramirez, P. Z., Salti, S., and Stefano, L. D. Deep learning on implicit neural representations of shapes, 2023.

Ma, J., Lu, E., Paiss, R., Zada, S., Holynski, A., Dekel, T., Curless, B., Rubinstein, M., and Cole, F. Vidpanos: Generative panoramic videos from casual panning videos. In *SIGGRAPH Asia 2024 Conference Papers*, December 2024.

Mescheder, L., Oechsle, M., Niemeyer, M., Nowozin, S., and Geiger, A. Occupancy networks: Learning 3d reconstruction in function space, 2019.

Mildenhall, B., Srinivasan, P. P., Tancik, M., Barron, J. T., Ramamoorthi, R., and Ng, R. Nerf: Representing scenes as neural radiance fields for view synthesis. In *European Conference on Computer Vision (ECCV)*, pp. 405–421. Springer, 2020. doi: 10.1007/978-3-030-58452-8_24.

Momenifar, M., Diao, E., Tarokh, V., and Bragg, A. D. A physics-informed vector quantized autoencoder for data compression of turbulent flow. In *2022 Data Compression Conference (DCC)*, pp. 01–10, 2022. doi: 10.1109/DCC52660.2022.00039.

Müller, T., Evans, A., Schied, C., and Keller, A. Instant neural graphics primitives with a multiresolution hash encoding. *ACM Trans. Graph.*, 41(4):102:1–102:15, July 2022. doi: 10.1145/3528223.3530127.

Ohana, R., McCabe, M., Meyer, L., Morel, R., Agocs, F., Beneitez, M., Berger, M., Burkhardt, B., Dalziel, S., Fielding, D., et al. The well: a large-scale collection of diverse physics simulations for machine learning. *Advances in Neural Information Processing Systems*, 37:44989–45037, 2024.

Page, J. Super-resolution of turbulence with dynamics in the loss. *Journal of Fluid Mechanics*, 1002:R3, 2025. doi: 10.1017/jfm.2024.1202.

Paischer, F., Galletti, G., Hornsby, W., Setinek, P., Zanisi, L., Carey, N., Pamela, S., and Brandstetter, J. In *Advances in Neural Information Processing Systems 38: Annual Conference on Neural Information Processing Systems 2025*, NeurIPS 2025, San Diego, CA, USA, December 02 - 07, 2025, 2025a.

Paischer, F., Hauzenberger, L., Schmied, T., Alkin, B., Deisenroth, M. P., and Hochreiter, S. Parameter efficient fine-tuning via explained variance adaptation, 2025b.

Park, J. J., Florence, P., Straub, J., Newcombe, R., and Lovegrove, S. Deep sdf: Learning continuous signed distance functions for shape representation, 2019.

Peebles, W. and Xie, S. Scalable diffusion models with transformers. In *2023 IEEE/CVF International Conference on Computer Vision (ICCV)*, pp. 4172–4182, 2023. doi: 10.1109/ICCV51070.2023.00387.

Peeters, A., Camenen, Y., Casson, F., Hornsby, W., Snodin, A., Strintzi, D., and Szepesi, G. The non-linear gyro-kinetic flux tube code gkw. *Computer Physics Communications*, 180(12):2650–2672, 2009. ISSN 0010-4655. doi: <https://doi.org/10.1016/j.cpc.2009.07.001>. 40 YEARS OF CPC: A celebratory issue focused on quality software for high performance, grid and novel computing architectures.

Qiu, Z., Wang, Z., Zheng, B., Huang, Z., Wen, K., Yang, S., Men, R., Yu, L., Huang, F., Huang, S., Liu, D., Zhou, J., and Lin, J. Gated attention for large language models: Non-linearity, sparsity, and attention-sink-free, 2025.

Rahaman, N., Baratin, A., Arpit, D., Draxler, F., Lin, M., Hamprecht, F. A., Bengio, Y., and Courville, A. On the spectral bias of neural networks, 2019.

Raissi, M., Perdikaris, P., and Karniadakis, G. E. Physics-informed neural networks: A deep learning framework for solving forward and inverse problems involving nonlinear partial differential equations. *Journal of Computational Physics*, 378:686–707, 2019. doi: 10.1016/j.jcp.2018.10.045.

Saragadam, V., LeJeune, D., Tan, J., Balakrishnan, G., Veeraraghavan, A., and Baraniuk, R. G. Wire: Wavelet implicit neural representations. In *Proceedings of the IEEE/CVF Conference on Computer Vision and Pattern Recognition (CVPR)*, 2023. arXiv preprint arXiv:2301.05187.

Serrano, L., Boudec, L. L., Koupaï, A. K., Wang, T. X., Yin, Y., Vittaut, J., and Gallinari, P. Operator learning with neural fields: Tackling pdes on general geometries. *CoRR*, abs/2306.07266, 2023. doi: 10.48550/ARXIV.2306.07266.

Siena, A. D., Bourdelle, C., Navarro, A. B., Merlo, G., Görler, T., Fransson, E., Polevoi, A., Kim, S. H., Koechl, F., Loarte, A., Fable, E., Angioni, C., Mantica, P., and Jenko, F. First global gyrokinetic profile predictions of iter burning plasma, 2025.

Sitzmann, V., Martel, J. N. P., Bergman, A. W., Lindell, D. B., and Wetzstein, G. Implicit neural representations with periodic activation functions. In *NeurIPS*, 2020. arXiv preprint arXiv:2006.09661.

Son, H., Jang, J. W., Han, W. J., and Hwang, H. J. Sobolev training for physics informed neural networks, 2021.

Su, J., Lu, Y., Pan, S., Murtadha, A., Wen, B., and Liu, Y. Roformer: Enhanced transformer with rotary position embedding, 2023.

Teney, D., Nicolicioiu, A., Hartmann, V., and Abbasnejad, E. Neural redshift: Random networks are not random functions, 2025.

Toshev, A. P., Galletti, G., Fritz, F., Adami, S., and Adams, N. A. Lagrangebench: A lagrangian fluid mechanics benchmarking suite, 2023.

Tskhakaya, D. The Particle-in-Cell Method, pp. 161–189. Springer Berlin Heidelberg, Berlin, Heidelberg, 2008. ISBN 978-3-540-74686-7. doi: 10.1007/978-3-540-74686-7_6.

van den Oord, A., Vinyals, O., and Kavukcuoglu, K. Neural discrete representation learning. In Advances in Neural Information Processing Systems (NeurIPS), volume 30, 2017.

Woo, S., Yun, J., and Kim, G. Meta-continual learning of neural fields, 2025.

Xie, Y., Takikawa, T., Saito, S., Litany, O., Yan, S., Khan, N., Tombari, F., Tompkin, J., Sitzmann, V., and Sridhar, S. Neural fields in visual computing and beyond. CoRR, abs/2111.11426, 2021.

Yan, Z., Tian, Y., Shi, X., Guo, P., Wang, P., and Zha, H. Continual neural mapping: Learning an implicit scene representation from sequential observations, 2021.

Yang, G., Luo, R., Yao, Q., Wang, P., and Zhang, J. Multi-scale super-resolution reconstruction of fluid flows with deep neural networks. arXiv preprint arXiv:2509.14721, 2025. Preprint.

A. Gyrokinetics

Gyrokinetics (Frieman & Chen, 1982; Krommes, 2012; Peeters et al., 2009) is a reduced form of Plasma kinetics that is computationally more efficient and can be used to locally simulate Plasma behavior within a so-called *flux tube* in the torus. Local gyrokinetics is a theoretical framework to study plasma behavior on perpendicular spatial scales comparable to the gyroradius, i.e., the radius of circular motion exhibited by charged particles in a magnetic field, and frequencies much lower than the particle cyclotron frequencies, i.e., the frequency at which charged particles spiral around magnetic field lines due to the Lorentz force. Gyrokinetics models the time evolution of electrons and ions via the distribution function f , which is based on 3D coordinates, their parallel and perpendicular velocities, together with the angle w.r.t. the field lines. However, the latter dimension is averaged out by modelling only the so-called guiding center of a particle instead of its gyral movement. Furthermore, instead of modelling the perpendicular velocity, usually only its magnitude is considered, which is also referred to as the magnetic moment μ . Hence, the 5D gyrokinetic distribution function can be written as $f = f(k_x, k_y, s, v_{\parallel}, \mu)$, where k_x and k_y are spectral coordinates, s is the toroidal coordinate along the field line, and v_{\parallel} the parallel velocity component. The perturbed time-evolution of f , for each species (ions and electrons), is governed by

$$\underbrace{\frac{\partial f}{\partial t} + (v_{\parallel} \mathbf{b} + \mathbf{v}_D) \cdot \nabla f - \frac{\mu B}{m} \frac{\mathbf{B} \cdot \nabla B}{B^2} \frac{\partial f}{\partial v_{\parallel}}}_{\text{Linear}} + \underbrace{\mathbf{v}_{\chi} \cdot \nabla f}_{\text{Nonlinear}} = S, \quad (9)$$

where $v_{\parallel} \mathbf{b}$ is the motion along magnetic field lines, $\mathbf{b} = \mathbf{B}/B$ is the unit vector along the magnetic field \mathbf{B} with magnitude B ², \mathbf{v}_D the magnetic drift due to gradients and curvature in \mathbf{B} , and \mathbf{v}_{χ} describes drifts arising from the $\mathbf{E} \times \mathbf{B}$ force, a key driver of plasma dynamics. Finally, S is the source term, the external supply of energy. The term $\mathbf{v}_{\chi} \cdot \nabla f$ models the nonlinear interaction between the distribution function f and its velocity space integral ϕ , and it describes turbulent advection. The resulting nonlinear coupling constitutes the computationally most expensive term.

A.1. Derivation of the Gyrokinetic equation

We begin with the Vlasov equation for the distribution function $f(\mathbf{r}, \mathbf{v}, t)$:

$$\frac{\partial f}{\partial t} + \mathbf{v} \cdot \nabla f + \frac{q}{m} (\mathbf{E} + \mathbf{v} \times \mathbf{B}) \cdot \nabla_{\mathbf{v}} f = 0 \quad (10)$$

The Vlasov equation describes the conservation of particles in phase space in the absence of collisions. Here, $\mathbf{r} = (x, y, z)$ and $\mathbf{v} = (v_x, v_y, v_z)$ correspond to coordinates in the spatial and the velocity domain, respectively. Hence the Vlasov equation is a 7D (including time) PDE representing the density of particles in phase space at position \mathbf{r} , velocity \mathbf{v} , and time. The term $\nabla_{\mathbf{v}} f$ describes the response of the distribution function to accelerations of particles and $\frac{q}{m} (\mathbf{E} + \mathbf{v} \times \mathbf{B})$ denotes the Lorentz force, which depends on particle charge q and mass m , as well as electric field \mathbf{E} and magnetic field \mathbf{B} . Finally, the advection (or convection) term $\mathbf{v} \nabla f$ describes transport of the distribution function through space due to velocities.

To derive the *gyrokinetic equation*, we transform from particle to guiding center coordinates $(\mathbf{R}, v_{\parallel}, \mu, \theta)$, where $\mu = \frac{mv_{\perp}^2}{2B}$ is the magnetic moment, θ the gyrophase (particle position around its guiding center as it gyrates along a field line), and \mathbf{R} is the coordinate of the guiding center.

Assuming the time scale L at which the background field changes is much longer than the gyroperiod (small Larmor radius $\rho \ll L$), we can *gyroaverage* to remove the dependency on the gyrophase θ :

$$\frac{\partial f}{\partial t} + \dot{\mathbf{R}} \cdot \nabla f + \dot{v}_{\parallel} \frac{\partial f}{\partial v_{\parallel}} = 0 \quad (11)$$

A.1.1. LINEAR TERMS

The unperturbed (background) motion of the guiding center is governed by:

$$\dot{\mathbf{R}} = v_{\parallel} \mathbf{b} + \mathbf{v}_D \quad (12)$$

$$\dot{v}_{\parallel} = -\frac{\mu}{m} \mathbf{b} \cdot \nabla B \quad (13)$$

²We adopt uppercase notation for vector fields \mathbf{E} and \mathbf{B} to adhere with literature.

Here, $\mathbf{b} = \mathbf{B}/B$ is the unit vector along the magnetic field, and \mathbf{v}_D represents magnetic drifts. Substituting into the kinetic equation yields

$$\frac{\partial \mathbf{f}}{\partial t} + (v_{\parallel} \mathbf{b} + \mathbf{v}_D) \cdot \nabla \mathbf{f} - \frac{\mu}{m} \mathbf{b} \cdot \nabla B \frac{\partial \mathbf{f}}{\partial v_{\parallel}} = 0 \quad (14)$$

We can express the magnetic gradient term using:

$$\mathbf{b} \cdot \nabla B = \frac{\mathbf{B} \cdot \nabla \mathbf{B}}{B} \quad (15)$$

so that:

$$\frac{\mu}{m} \mathbf{b} \cdot \nabla B = \frac{\mu B}{m} \frac{\mathbf{B} \cdot \nabla \mathbf{B}}{\mathbf{B}^2} \quad (16)$$

A.1.2. NONLINEAR TERM

Fluctuating electromagnetic potentials $\delta\phi, \delta\mathbf{A}$ induce $\mathbf{E} \times \mathbf{B}$ and magnetic flutter drifts. We define the gyroaveraged generalized potential as

$$\chi = \langle \phi - \frac{v_{\parallel}}{c} A_{\parallel} \rangle, \quad (17)$$

where A_{\parallel} is the parallel component of the vector potential, $\langle \cdot \rangle$ denotes the gyroaverage, and c is the speed of light, which is added to ensure correct units. ϕ is the electrostatic potential, the computation of which involves an integral of \mathbf{f} over the velocity space (see eq. 1.41 in the GKW manual³ for a complete description).

This gives rise to the drift

$$\mathbf{v}_{\chi} = \frac{c}{B} \mathbf{b} \times \nabla \chi, \quad (18)$$

and yields the nonlinear advection term $\mathbf{v}_{\chi} \cdot \nabla \mathbf{f}$.

A.1.3. FINAL EQUATION

We arrive at the gyrokinetic equation in split form:

$$\frac{\partial \mathbf{f}}{\partial t} + (v_{\parallel} \mathbf{b} + \mathbf{v}_D) \cdot \nabla \mathbf{f} - \frac{\mu B}{m} \frac{\mathbf{B} \cdot \nabla B}{B^2} \frac{\partial \mathbf{f}}{\partial v_{\parallel}} + \mathbf{v}_{\chi} \cdot \nabla \mathbf{f} = S \quad (19)$$

Here, S represents external sources, collisions, or other drive terms. To enhance the tractability of Equation (9), the distribution function \mathbf{f} is usually split into equilibrium and perturbation terms

$$\mathbf{f} = \mathbf{f}_0 + \delta \mathbf{f} = \underbrace{\mathbf{f}_0 - \frac{Z\phi}{T} \mathbf{f}_0}_{\text{Adiabatic}} + \underbrace{\frac{\partial h}{\partial t}}_{\text{Kinetic}}, \quad (20)$$

where \mathbf{f}_0 is a background or equilibrium distribution function, T the particle temperature, Z the particle charge, ϕ the electrostatic potential, and $\delta \mathbf{f}$ the total perturbation to the distribution function, which comprises of *adiabatic* and *kinetic* response. The adiabatic term describes rapid and passive responses to the electrostatic potential that do not contribute to turbulent transport, while the kinetic term governs irreversible dynamics that facilitate turbulence. Numerical codes, such as GKW (Peeters et al., 2009), rely on solving for $\delta \mathbf{f}$ instead of \mathbf{f} . A common simplification is to assume that electrons are adiabatic, which allows us to neglect the kinetic term in the respective $\delta \mathbf{f}$. Hence, the respective \mathbf{f} for electrons (\mathbf{f}_e) does not need to be modelled, effectively halving the computational cost.

B. Dataset

The simulations used for both the autoencoder training (26 trajectories) and the evaluation (10 trajectories) are generated with the numerical code GKW (Peeters et al., 2009). They are sampled by varying four parameters: R/L_t , R/L_n , \hat{s} , and q , which significantly affect emerging turbulence in the Plasma.

³<https://bitbucket.org/gkw/gkw/src/develop/doc/manual/>

- R/L_t is the ion temperature gradient, which is the main driver of turbulence.
- R/L_n is the density gradient, whose effect is less pronounced. It can have a stabilizing effect, but can sometimes also lead to increased turbulence.
- \hat{s} denotes magnetic shearing, hence it usually has a stabilizing effect as more magnetic shearing results in better isolation of the Plasma.
- q denotes the so-called safety factor, which is the inverse of the rotational transform and describes how often a particle takes a poloidal turn before taking a toroidal turn.

We specify the ranges for sampling the four parameters as $R/L_T \in [1, 12]$, $R/L_n \in [1, 7]$, $q \in [1, 9]$, and $\hat{s} \in [0.5, 5]$. Additionally, we also vary the noise amplitude of the initial condition (within $[1e-5, 1e-3]$).

To make storage more feasible, simulations are time-coarsened by saving snapshot every 60. Each GKW run with the specified configurations takes around ~ 6 hours (76 cores, Intel Ice Lake 4.1GHz CPU) and ~ 60 GBs of storage.

C. Implementation details

C.1. Metrics

We evaluate reconstruction with spatial and physical metrics. Since gyrokinetic data is complex-valued, we can also apply complex-generalizations of common metrics.

Complex L1 Loss. Given two complex-valued fields $z_1, z_2 \in \mathbb{C}^N$, the complex L1 loss is:

$$cL1(z_1, z_2) = \langle |\Re(z_1 - z_2)| + |\Im(z_1 - z_2)| \rangle = \langle |z_1 - z_2|_1 \rangle$$

where $\langle \cdot \rangle$ denotes the average over all dimensions and $|\cdot|_1$ is the L1 norm of the complex difference.

Wasserstein Distance. The Wasserstein distance measures the minimum cost of transforming one probability distribution into another, where the cost is proportional to the distance the probability mass must be moved. It provides a meaningful metric to compare distributions even when they have non-overlapping support, making it particularly useful in machine learning and optimal transport problems. In our case, we normalize the spectra so that their total sum is one, ensuring they represent comparable probability distributions. The Wasserstein distance between two probability distributions P and Q is defined as:

$$W_p(P, Q) = \left(\inf_{\gamma \in \Gamma(P, Q)} \int \|x - y\|^p d\gamma(x, y) \right)^{\frac{1}{p}}$$

Peak Signal-to-Noise Ratio. Peak signal-to-noise ratio (PSNR) quantifies the ratio between the maximum possible power of a signal and the power of noise corrupting its representation, typically expressed in decibels (dB) due to the wide dynamic range of signals.

$$\text{PSNR}(x_1, x_2) = 10 \cdot \log_{10} \left(\frac{\max(x_1)^2}{\text{MSE}(x_1, x_2)} \right)$$

where $\text{MSE}(x_1, x_2)$ is the mean squared error between the real-valued fields x_1 and x_2 . The PSNR for complex-valued fields we defined as:

$$\text{cPSNR}(z_1, z_2) = 10 \cdot \log_{10} \left(\frac{\max(|z_1|)^2}{\text{cMSE}(z_1, z_2)} \right)$$

Bits Per Pixel (BPP). The BPP measures compression efficiency. Given a discrete representation of a field z and its compressed encoding, the bits per pixel is defined as

$$\text{BPP} = \frac{\text{Total number of bits used to encode } z}{\text{Number of spatial points in } z}.$$

Optical Flow and End-Point Error (EPE). Optical flow estimates the apparent motion between consecutive frames by computing spatial gradients and temporal derivatives. Applying the standard video algorithms to 5D data by reshaping or flattening dimensions introduces physical discontinuities and artificial flow boundaries, resulting in non-existent "ghost" flows. Instead, we extend the popular Horn–Schunck method (Horn & Schunck, 1981) to 5D, which computes the optical flow field directly on the 5D grid. In this case, the optical flow is a velocity vector field $\mathbf{u} = (u_{v\parallel}, u_\mu, u_s, u_x, u_y)$, resulting in 5 components per grid location.

For two consecutive frames $x(t)$ and $x(t+1)$, we compute the temporal derivative $\delta_t x$ and the spatial gradient vector $\nabla x = (\partial_{v\parallel} x, \partial_\mu x, \partial_s x, \partial_x x, \partial_y x)$ using finite differences on the temporal mid-point average. The full Horn–Schunck method enforces global smoothness by iteratively minimizing an energy functional, balancing brightness constancy with a smoothness term weighted by α . This formulation yields the following iterative update rule for the k -th iteration:

$$\mathbf{u}^{(k+1)} = \bar{\mathbf{u}}^{(k)} - \frac{\nabla x (\nabla x \cdot \bar{\mathbf{u}}^{(k)} + \Delta x)}{\alpha^2 + \|\nabla x\|^2},$$

where $\bar{\mathbf{u}}^{(k)}$ represents the local average of the flow vectors from the previous iteration. This average is computed via 5D convolution using a star kernel K . It assigns a uniform weight of 1/10 to the 10 immediate neighbors (2 neighbors, 5 dimensions) along the spatial dimensions. The pseudocode we use for the 5D Horn–Schunck is in Algorithm 1. Without the smoothing step it's the special case of *normal flow*, capturing motion strictly in the direction of the gradient (e.g. disregarding diagonal shifts).

```

1  def horn_schunck( $x$  (5+1D data),  $\alpha$  (regularization),  $N$  (iters)):
2       $\delta_t x = x_{t+1} - x_t$  # temporal gradient (assume regular frame-rate)
3       $\nabla x = \text{gradient}(0.5(x_t + x_{t+1}))$  # spatial gradient
4       $D = \alpha^2 + \|\nabla x\|^2$  # normalization factor
5      # iterative smoothing
6      kernel = star(neighbors=2 * 5, kernel_size=3)
7       $u \leftarrow 0$ 
8      for  $k = 1$  to  $N$ :
9          # global smoothness via local averaging
10          $\bar{u} = \text{convolve}(u, \text{kernel})$ 
11         # Update flow (project temporal change onto spatial gradient)
12          $\text{project} = (\nabla x \cdot \bar{u} + x_t)/D$ 
13          $u \leftarrow \bar{u} - \nabla x \cdot \text{project}$ 
14
    return  $u$ 

```

Listing 1. Generalized 5D Horn–Schunck

Given two sequences of N frames, the End-Point Error (EPE) (Baker et al., 2011) is defined as the mean squared Euclidean difference between the predicted flow vectors $\mathbf{F}_{pred}^{(i,j)}$ and the target flow vectors $\mathbf{F}_{tgt}^{(i,j)}$ over all M grid points and time steps:

$$\text{EPE} = \frac{1}{N \cdot M} \sum_{i=1}^N \sum_{j=1}^M \|\mathbf{F}_{pred}^{(i,j)} - \mathbf{F}_{tgt}^{(i,j)}\|_2^2.$$

C.2. Traditional compression

In the following paragraphs we briefly describe how the traditional compressions were implemented.

ZFP Compression. ZFP Lindstrom (2014) is a compression library for numerical arrays designed for fast random access. It partitions the data into small blocks (typically $4 \times 4 \times 4$ elements for 3D data) and transforms them into a decorrelated representation using an orthogonal block transform. The transformed coefficients are quantized according to a user-specified tolerance, then entropy-coded to produce a compact bitstream. High-speed random access and both lossy and lossless are possible, making ZFP a very common choice for scientific data storage.

We rearrange \mathbf{f} into a 3D array as $((v\parallel \times \mu) \times (s \times y) \times x)$ for ZFP block-based compression scheme (up to 3D), and compress with ZFP with a specified absolute error tolerance. The compressed representation is a compact byte representation. Reconstruction is performed by decompressing with ZFP and reshaping the output back to the original tensor layout.

Wavelet Compression. Discrete wavelet transform (DWT) is applied using the level 1 Haar wavelet. The multi-dimensional array is decomposed into wavelets (coefficient and slices). To achieve lossy compression, coefficients are pruned based on a fixed threshold dependent on the desired compression ratio, effectively discarding small high-frequency components. Reconstruction is performed by inverting the DWT.

Principal Component Analysis Compression. \mathbf{f} is reshaped into a 2D array $((v_{\parallel} \cdot \mu \cdot s) \times (x \cdot y))$, by rearranging together the velocity space v_{\parallel}, μ with the field line s and the spatial coordinates x, y . PCA is applied on the flattened spatial components, retaining a fixed number of principal components dependent on the desired compression ratio ($N = 2$ for $1,000 \times$ from Table 1). The compressed representation consists of the principal components, the mean vector, and the explained variance. Reconstruction is achieved by projecting back to the original space, followed by reshaping to the original dimensions.

JPEG2000 Compression. \mathbf{f} is first reshaped into a 2D image-like representation of shape $((v_{\parallel} \cdot \mu \cdot s) \times (x \cdot y))$, by flattening the velocity space and spatial dimensions. Each channel is independently normalized to the $[0, 1]$ range and quantized to 16-bit unsigned integers. The images are then encoded using the JPEG2000 standard (Christopoulos et al., 2000) at a target quality factor Q that determines the compression ratio. The compressed representation consists of the codestream size and channelwise normalization statistics (minimum and maximum). Reconstruction is performed by decoding the JPEG2000 bitstream, rescaling back to floating-point values, and unflattening back to the original tensor dimensions.

C.3. VAPOR

VAPOR (Choi et al., 2021) combines a VQ-VAE van den Oord et al. (2017) compressor and a Fourier Neural Operator (FNO) (Li et al., 2021) Refiner sequentially. The VQ-VAE provides extreme compression by reducing the size of the original data, and the FNO Refiner then refines the VQ-VAE’s coarse output to restore fidelity, achieving both high compression and high accuracy. We utilize a VQ-VAE with Exponential Moving Average (EMA) updates to compress the data \mathbf{f} . This forms the first stage of the overall architecture. The FNO refiner stage uses a residual structure to efficiently learn and apply the high-frequency corrections needed to match the ground-truth solution, taking the VQ-VAE initial reconstruction as input.

Finally, a core component of Choi et al. (2021) is the specialized physics loss $\mathcal{L}_{\text{physics}}$, employed to enforce conservation laws. This loss computes the MSE between the predicted and ground-truth values of density, momentum, and energy:

$$\begin{aligned} \mathcal{L}_{\text{physics}} = & \text{MSE} \left(\sum_{v_{\parallel}, v_{\perp}} \mathbf{f}_{\text{pred}}, \sum_{v_{\parallel}, v_{\perp}} \mathbf{f}_{\text{gt}} \right) + \text{MSE} \left(\sum_{v_{\parallel}, v_{\perp}} \mathbf{f}_{\text{pred}} v_{\parallel}, \sum_{v_{\parallel}, v_{\perp}} \mathbf{f}_{\text{gt}} v_{\parallel} \right) \\ & + \text{MSE} \left(\sum_{v_{\parallel}, v_{\perp}} \mathbf{f}_{\text{pred}} \frac{1}{2} m_s v_{\parallel}^2, \sum_{v_{\parallel}, v_{\perp}} \mathbf{f}_{\text{gt}} \frac{1}{2} m_s v_{\parallel}^2 \right). \end{aligned}$$

This loss is added to the standard reconstruction and VQ losses during training to obtain the final VAPOR loss: $\mathcal{L} = \mathcal{L}_{\text{recon}} + \mathcal{L}_{\text{VQ}} + \mathcal{L}_{\text{physics}}$. Results in Table 6.

C.4. Autoencoders

Architecture and Conditioning. The autoencoder and VQ-VAE baselines are built on a 5D Swin Transformer architecture (Galletti et al., 2025; Paischer et al., 2025a), which extends the shifted window attention mechanism to handle

Table 6. VAPOR results on the same setup as Table 1.

		Compression \mathbf{f}		Integrals Q, ϕ		Turbulence $Q^{\text{spec}}, k_y^{\text{spec}}$	
	CR	PSNR \uparrow	EPE \downarrow	L1(Q) \downarrow	PSNR(ϕ) \uparrow	WD($\overline{k_y^{\text{spec}}}$) \downarrow	WD($\overline{Q^{\text{spec}}}$) \downarrow
VAPOR	$64 \times$	29.52 ± 1.36	0.123 ± 0.07	90.75 ± 48.41	-13.96 ± 5.97	0.020 ± 0.01	0.010 ± 0.00
PINC-NF	$1167 \times$	35.76 ± 1.38	0.037 ± 0.02	2.18 ± 8.33	13.50 ± 4.44	0.006 ± 0.00	0.015 ± 0.00
AE + EVA	$716 \times$	35.64 ± 2.03	0.063 ± 0.05	15.01 ± 16.42	6.72 ± 4.98	0.016 ± 0.01	0.012 ± 0.01

high-dimensional scientific data. Figure 5 illustrates the 5D windowed multi-head self-attention (W-MSA) and shifted windowed multi-head self-attention (SW-MSA) layers, where blocks of the same color indicate the receptive field of local attention within each window. Our implementation incorporates several stability and performance enhancements: gated attention mechanisms (Qiu et al., 2025) for improved training stability, combined positional encodings using both Relative Positional Bias (Liu et al., 2021) and Rotary Position Embedding (RoPE) (Su et al., 2023) to capture spatial relationships across all five dimensions, and GELU activations (Hendrycks & Gimpel, 2023) throughout the network. Each model uses four Swin blocks with 16 attention heads, followed by a single downsampling level before the bottleneck. All models are conditioned on four key gyrokinetic parameters: the ion temperature gradient (R/L_t), density gradient (R/L_n), magnetic shear (\hat{s}), and safety factor (q). Conditioning is implemented via DiT-style modulation (Peebles & Xie, 2023), where conditioning embeddings provide scale, shift, and gating parameters for each transformer layer, enabling physics-aware feature adaptation.

Data Preprocessing.

The 5D distribution function $[v_{\parallel}, \mu, s, x, y]$ is represented as complex values with real and imaginary components, initially providing two channels. We apply two key preprocessing steps that affect the channel structure. First, we decomposes each field into zonal flow ($k_y = 0$ mode) and turbulent fluctuation components by computing the mean across the k_y dimension and concatenating the zonal flow and turbulent fluctuation, doubling the channels to four. This separation is essential as zonal flows exhibit fundamentally different physics from turbulent modes. Second, we reshape the magnetic moment dimension μ , into the channel dimension, expanding from four to 32 channels. This allows independent processing of each μ slice.

Compression Configurations. We evaluate multiple compression ratios by varying patch and window sizes. For autoencoders, three configurations achieve compression ratios of 302, 1208, and 2865 using patch sizes $(2, 0, 2, 5, 2)$, $(4, 0, 2, 5, 4)$, and $(6, 0, 3, 5, 6)$ with corresponding window sizes $(8, 0, 4, 9, 8)$, $(4, 0, 4, 9, 4)$, and $(6, 0, 6, 9, 6)$. The zero in the second position corresponds to the μ dimension, which is not spatially patched due to the decoupling preprocessing step. All variants use latent dimension 1024, and compress in a last linear projection to the bottleneck dimension of 32.

VQ-VAE Variants. VQ-VAE uses the same spatial compression configurations but replaces the continuous bottleneck with vector quantization using the implementation from `vector-quantize-pytorch`⁴. The bottleneck projects to 128-dimensional embeddings, which are quantized using a codebook of 8192 vectors (see Table 7 for complete hyperparameters). The codebook uses exponential moving average updates with a decay rate of 0.99 and employs entropy regularization to encourage codebook utilization. This yields much higher compression ratios of 19342, 25789, and 77368 for the three spatial configurations, as quantized codes can be stored as integers (int16 for codebook size of 8192) rather than float32 values.

Training Strategy. Training follows a two-stage approach to ensure stability. For all experiments we use Muon optimizer (Jordan et al., 2024) with a cosine scheduler and a minimum learning rate of 4×10^{-6} , and weight decay of 1×10^{-5} . *Stage 1* (200 epochs, batchsize=16, lr= 2×10^{-4}) trains the base autoencoder using only $\mathcal{L}_{\text{recon}}$ (cMSE). *Stage 2.1* (100 epochs, batchsize=16, lr= 2×10^{-4}) applies Explained Variance Adaptation (EVA) (Paischer et al., 2025b), which injects LoRA (Hu et al., 2022) weights ($r = 64$, $\alpha = 1$, $\rho = 2.0$, $\tau = 0.99$) into MLP layers while freezing the Stage 1 trained backbone. The loss function switches to cL1 for reconstruction ($\mathcal{L}_{\text{recon}}$ weighted by 10.0) and introduces physics-informed losses: integral losses (\mathcal{L}_Q , \mathcal{L}_{ϕ}) using scale normalization (scale is calculated over training dataset statistics), while spectral losses (\mathcal{L}_{k_y} , $\mathcal{L}_{Q^{\text{spec}}}$) employ sum-normalization followed by log-space L1 loss. All physics-informed loss terms are weighted equally at 1.0, with the VQ-VAE commitment loss also weighted by a factor of 10.0 to match the reconstruction weight. Critically, monotonicity constraints (\mathcal{L}_{iso}) are disabled. *Stage 2.2* (20 epochs,

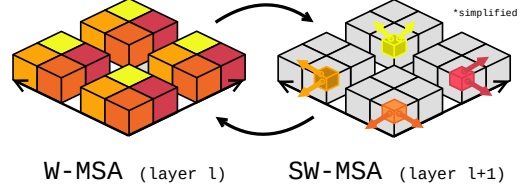


Figure 5. 5D swin attention.

Table 7. VQ-VAE vector quantization hyperparameters.

Parameter	Value
Codebook size	8192
Embedding dimension	128
Commitment weight	0.3
Codebook type	Euclidean
EMA decay	0.99
Entropy loss weight	0.01
Dead code threshold	2

⁴<https://github.com/lucidrains/vector-quantize-pytorch>

batchsize=16, lr=2 \times 10⁻⁴) continues with identical settings but enables monotonicity losses ($\mathcal{L}_{\text{iso}}(k_y^{\text{spec,pred}})$, $\mathcal{L}_{\text{iso}}(Q^{\text{spec,pred}})$) to enforce physical constraints only after stable physics-informed reconstruction is achieved.

Training Stabilization. End-to-end training of autoencoders with physics-informed neural compression (PINC) losses proves highly unstable due to the conflicting optimization objectives and varying loss magnitudes. The physics-informed terms (\mathcal{L}_Q , \mathcal{L}_ϕ , \mathcal{L}_{k_y} , $\mathcal{L}_{Q^{\text{spec}}}$) exhibit severe fluctuations during early training when reconstruction quality is poor, causing certain loss components to dominate the overall objective and destabilizing the learning process. This necessitates the staged training approach, where reconstruction capability is first established before introducing physics constraints.

Multi-objective Optimization Challenges. We investigated several multi-objective optimization strategies to enable stable end-to-end training. Gradient normalization methods (Chen et al., 2018), while theoretically appealing, proved computationally prohibitive for our large-scale models, consistently causing out-of-memory errors during backpropagation. Conflict-Free Inverse Gradients (ConFIG) Liu et al. (2024) attempts to resolve conflicting optimization objectives by computing gradient directions that minimize conflicts between tasks through least-squares solutions. However, ConFIG relies on computing stable gradient statistics over multiple training steps to determine optimal gradient directions. When physics-informed losses are computed on poorly reconstructed distribution functions, these losses exhibit extreme fluctuations that prevent ConFIG from establishing stable gradient statistics. The method’s gradient balancing becomes ineffective when the underlying loss landscape is highly unstable, as the computed conflict-free directions become unreliable due to the volatile nature of the physics-informed terms during early training phases.

Hyperparameter Search Limitations. The computational cost of autoencoder training further complicates optimization. Each full training run requires multiple days on high-end GPUs, making systematic hyperparameter search for end-to-end training impractical. The search space includes not only standard hyperparameters (learning rates, batch sizes, architectural choices) but also the relative weighting of several distinct loss components, creating a prohibitively large optimization landscape. This computational constraint reinforces the necessity of our staged approach, which reduces the hyperparameter search to manageable subspaces for each training phase.

Codebook usage and Entropy Encoding. The VQ-VAE quantizes the continuous latent space into discrete integer indices (*codes*) ranging from 0 to the codebook size. Standard storage uses fixed-width encoding $\log_2(8192) = 13$ bits per code. However, empirical analysis reveals non-uniform usage: frequent codes dominate (common turbulent structures), while rare codes occur sporadically. This imbalance enables lossless compression via variable-length entropy coding. Our VQ-VAE achieves 71.4% codebook utilization (5846/8192 entries). The sorted codebook frequencies follow Zipf’s law, which suggest common flow patterns use frequent codes, while rare events retain dedicated codes. Further, we measure this redundancy using Shannon entropy $-\sum_i p_i \log_2(p_i)$ where p_i is the empirical probability of code i . Our dataset yields $H \approx 10.5$ bits, indicating that optimal encoding requires only 10.5 bits per code on average, compared to the 13-bit fixed-width baseline. On our test set, Huffman encoding (Huffman, 1952) achieves 1.56 \times additional compression over fixed-width storage, reducing average code length from 13 to 10.7 bits per code. Combined with VQ-VAE quantazation (77368 \times), the total pipelines achieves 121492 \times compression, going from 723.5GB (uncompressed) to 5.96MB (VQ-VAE + Huffman), instead of 9.32MB (VQ-VAE).

C.5. Neural fields

Neural fields are trained by representing the distribution function as a continuous signal, taking coordinates as inputs. A dataset consists, for a given simulation, of the 5D density function f at a specific timestep, and the 5D grid coordinates of each cell. Data normalization is applied both to the field values and to the coordinates.

An MLP with SiLU activations (Elfwing et al., 2017), 64 hidden dimension, five layers with skip connections and using a discrete hash to map matrix indices to learnable embeddings is optimized using AdamW (Loshchilov & Hutter, 2019), with cosine annealing learning rate scheduling decaying the learning rate from 5e -3 to 1e -12 and . Auxiliary optimizers can be used for additional integral losses, also with their scheduler that decays learning rate from 1e -5 to 1e -12 . The neural field training loop iterates over batches of (2048) coordinates and field values. On a first pass of 20 epochs, the loss $\mathcal{L}_{\text{recon}}$ from Equation (5) is fitted. Auxiliary integral losses are trained of such a pretrained model for 100 more epochs, with the whole 5D field as batch.

ConFIG ablations. We ablate multi-objective balancing methods such as Conflict-Free Inverse Gradients by Liu et al.

(2024) to attempt to stabilize training on the PINC loss terms. Table 8 compares AdamW training (as reported in Table 1) and neural fields complemented with momentum ConFIG with ordered loss selector. Results are similar, with regular AdamW achieving better physical losses and ConFIG being more stable overall.

Table 8. Ablations of NF trained with AdamW and Conflict-Free Inverse Gradients.

	CR	Compression f			Integrals Q, ϕ		Turbulence $Q^{\text{spec}}, k_y^{\text{spec}}$	
		L1 \downarrow	PSNR \uparrow	BBP \downarrow	L1(Q) \downarrow	PSNR(ϕ) \downarrow	WD(k_y^{spec}) \downarrow	WD(\bar{Q}^{spec}) \downarrow
PINC-NF (AdamW)	1163 \times	0.32	36.29	0.165	9.75	14.53	0.0057	0.0170
PINC-NF (SGD+ConFIG)	1163 \times	0.29	37.18	0.165	44.23	6.35	0.0164	0.0163

Neural field ablations. A broad range of architectures was explored, starting from SIREN (Sitzmann et al., 2020), WIRE Saragadam et al. (2023) and an MLP with different activations (Fukushima, 1969; Hendrycks & Gimpel, 2023; Elfwing et al., 2017). Table 9 summarizes the search space.

Table 9. Neural field search space summary. w_0 values are only for SIREN and WIRE architectures.

Knob	Range
Activations	Sine, Gabor, ReLU, SiLU, GELU
Coordinate embedding	Linear, SinCos, Discrete
w_0^{initial}	0.1, 0.5, 1.0
w_0^{hidden}	0.5, 2.0, 10.0
Skip connections	Yes, No
Learning rate	$1e-2, 5e-3$

An extensive grid search search was conducted evaluating every combination from Table 9 in the $\sim 1,000 \times$ compression regime, on 12 randomly sampled density fields f from four different trajectories. For simplicity we use PSNR of f as the selection metric. All models are trained for 10 epochs using the AdamW optimizer Loshchilov & Hutter (2019) with a batch size of 2048. A total of $12 \cdot 36$ (SIREN) + $12 \cdot 18$ (WIRE) + $12 \cdot 18$ (MLP) = 864 neural fields were trained for this ablation. The results from Tables 10, 12, and 11 suggest that MLP with SiLU activation, skip connections and discrete index embedding is the most performant setup, as well as the fastest and easiest to tune.

Table 10. MLP grid search combinations.

Activation	Embedding	Skip	Learning rate	f PSNR
SiLU	Discrete	Yes	$5e-3$	40.53
GELU	Discrete	Yes	$5e-3$	40.12
SiLU	Discrete	No	$5e-3$	40.11
GELU	Discrete	No	$5e-3$	39.96
ReLU	Discrete	Yes	$5e-3$	39.24
ReLU	Discrete	No	$5e-3$	38.83
GELU	Linear	No	$5e-3$	37.06
SiLU	SinCos	No	$5e-3$	36.88
GELU	SinCos	No	$5e-3$	36.78
GELU	Linear	Yes	$5e-3$	36.7
SiLU	Linear	No	$5e-3$	36.47
GELU	SinCos	Yes	$5e-3$	36.44
SiLU	Linear	Yes	$5e-3$	36.09
SiLU	SinCos	Yes	$5e-3$	35.18
ReLU	SinCos	Yes	$5e-3$	35.1
ReLU	SinCos	No	$5e-3$	34.68
ReLU	Linear	No	$5e-3$	34.45
ReLU	Linear	Yes	$5e-3$	34.4

Table 11. WIRE grid search combinations.

Embedding	w_0^{initial}	w_0^{hidden}	Learning rate	f	PSNR
Discrete	0.5	2.0	$1e-2$	29.33	
Discrete	0.1	2.0	$1e-2$	27.96	
Discrete	0.5	0.5	$1e-2$	27.9	
Discrete	0.1	0.5	$1e-2$	27.83	
Linear	0.1	2.0	$1e-2$	24.16	
Linear	0.1	5.0	$1e-2$	24.16	
Linear	0.1	0.5	$1e-2$	24.16	
Linear	0.5	0.5	$1e-2$	24.16	
Linear	0.5	2.0	$1e-2$	24.16	
Linear	0.5	5.0	$1e-2$	24.16	
Discrete	1.0	0.5	$1e-2$	7.65	
Discrete	1.0	2.0	$1e-2$	7.34	
Linear	1.0	0.5	$1e-2$	6.04	
Linear	1.0	2.0	$1e-2$	6.04	
Linear	1.0	5.0	$1e-2$	6.04	
Discrete	0.1	5.0	$1e-2$	nan	
Discrete	0.5	5.0	$1e-2$	nan	
Discrete	1.0	5.0	$1e-2$	nan	

Table 12. SIREN grid search combinations.

Embedding	w_0^{initial}	w_0^{hidden}	Skip	Learning rate	f PSNR
Discrete	0.1	0.5	Yes	5e-3	40.48
Discrete	0.5	0.5	Yes	5e-3	40.34
Discrete	0.5	0.5	No	5e-3	40.04
Discrete	0.1	0.5	No	5e-3	39.97
SinCos	0.5	2.0	Yes	5e-3	38.24
SinCos	0.1	2.0	Yes	5e-3	38.19
SinCos	0.5	0.5	No	5e-3	37.22
SinCos	0.1	0.5	No	5e-3	37.2
SinCos	0.1	0.5	Yes	5e-3	36.23
SinCos	0.5	0.5	Yes	5e-3	36.23
SinCos	0.1	2.0	No	5e-3	32.58
Discrete	0.1	2.0	No	5e-3	29.41
SinCos	0.1	5.0	Yes	5e-3	24.16
SinCos	0.1	5.0	No	5e-3	24.16
Discrete	0.1	5.0	No	5e-3	24.16
Discrete	0.1	2.0	Yes	5e-3	24.16
Discrete	0.5	2.0	Yes	5e-3	24.16
Discrete	0.1	5.0	Yes	5e-3	24.16
Discrete	1.0	0.5	Yes	5e-3	10.1
Discrete	1.0	0.5	No	5e-3	10.03
SinCos	1.0	2.0	Yes	5e-3	9.57
SinCos	1.0	0.5	No	5e-3	9.29
SinCos	1.0	0.5	Yes	5e-3	9.04
SinCos	1.0	2.0	No	5e-3	8.74
SinCos	0.5	2.0	No	5e-3	8.43
Discrete	1.0	2.0	No	5e-3	6.99
Discrete	0.5	2.0	No	5e-3	6.94
Discrete	1.0	2.0	Yes	5e-3	6.08
SinCos	1.0	5.0	Yes	5e-3	6.04
SinCos	0.5	5.0	Yes	5e-3	6.04
Discrete	0.5	5.0	No	5e-3	6.04
SinCos	1.0	5.0	No	5e-3	6.04
Discrete	1.0	5.0	No	5e-3	6.04
SinCos	0.5	5.0	No	5e-3	6.04
Discrete	1.0	5.0	Yes	5e-3	6.04
Discrete	0.5	5.0	Yes	5e-3	6.04

C.6. Extra results

Table 13. Missing metrics from Table 1. Evaluation on 420 total f s (20 different turbulent trajectories, 21 random time snapshots), sampled in the statistically steady phase, same setup as Table 1. Errors in data space.

	Compression f		Integrals ϕ		Turbulence Q^{spec} , k_y^{spec}		
	L1(f) \downarrow	BPP	L1(ϕ) \downarrow	PC(k_y^{spec}) \uparrow	PC(Q^{spec}) \uparrow	L1(k_y^{spec}) \uparrow	L1(Q^{spec}) \uparrow
ZFP	0.72 ± 0.19	0.036	$1.11 \times 10^3 \pm 1.06 \times 10^3$	0.9287 ± 0.10	-0.0053 ± 0.73	$4.37 \times 10^5 \pm 8.59 \times 10^5$	107.51 ± 40.90
Wavelet	0.50 ± 0.12	0.034	$7.49 \times 10^2 \pm 8.54 \times 10^2$	0.9291 ± 0.10	-0.9628 ± 0.05	$3.90 \times 10^5 \pm 8.27 \times 10^5$	107.74 ± 40.99
PCA	0.52 ± 0.14	0.031	$4.46 \times 10^2 \pm 4.19 \times 10^2$	0.9290 ± 0.10	0.8705 ± 0.38	$9.95 \times 10^4 \pm 1.56 \times 10^5$	67.45 ± 24.02
JPEG2000	0.51 ± 0.13	0.032	$1.78 \times 10^3 \pm 1.52 \times 10^3$	0.9280 ± 0.10	-0.0363 ± 0.82	$8.63 \times 10^5 \pm 1.27 \times 10^6$	103.91 ± 36.75
VAPOR	0.88 ± 0.25	0.5	$7.80 \times 10^2 \pm 6.60 \times 10^2$	0.9280 ± 0.10	0.9804 ± 0.01	$1.62 \times 10^5 \pm 2.80 \times 10^5$	91.95 ± 40.39
NF	0.33 ± 0.09	0.027	$1.37 \times 10^2 \pm 1.26 \times 10^2$	0.9392 ± 0.08	0.9735 ± 0.02	$6.07 \times 10^3 \pm 1.01 \times 10^4$	61.50 ± 14.96
PINC-NF	0.37 ± 0.08	0.027	26.52 ± 24.35	0.9870 ± 0.02	0.9797 ± 0.02	$2.37 \times 10^2 \pm 3.92 \times 10^2$	49.48 ± 15.88
AE + EVA	0.45 ± 0.17	0.045	73.13 ± 74.30	0.9419 ± 0.07	0.9785 ± 0.03	$1.63 \times 10^3 \pm 3.83 \times 10^3$	48.48 ± 33.26
VQ-VAE + EVA	0.54 ± 0.20	0.0004	56.11 ± 37.12	0.9437 ± 0.06	0.7888 ± 0.22	$5.35 \times 10^2 \pm 8.59 \times 10^2$	73.47 ± 46.51

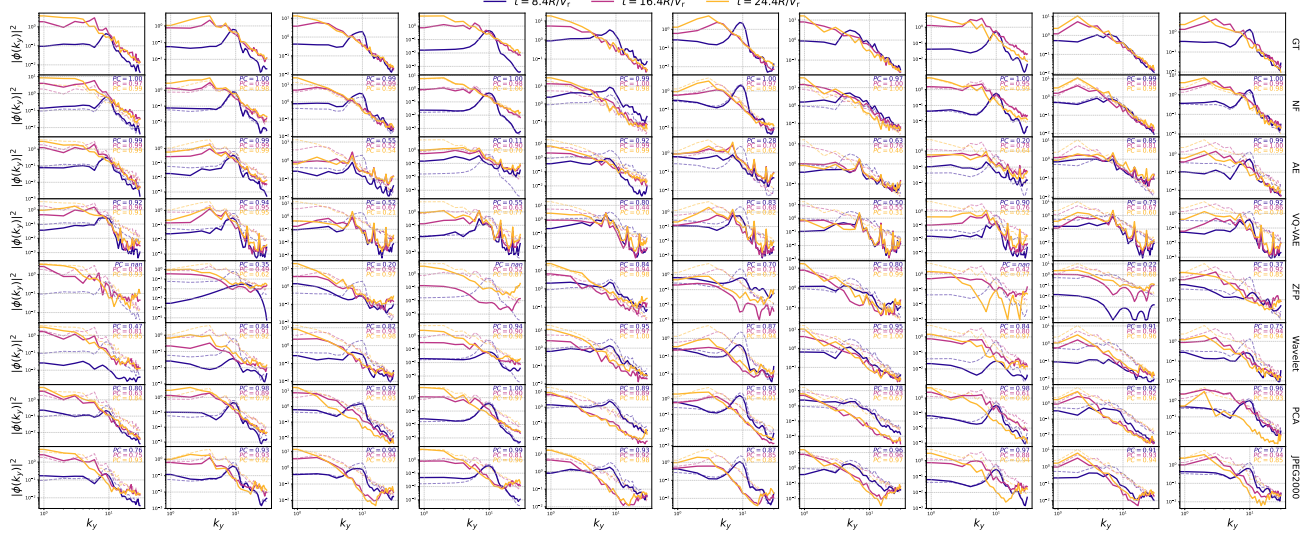


Figure 6. Extra models for the energy cascade (left Figure 4). The three time snapshots at $[8.4, 16.4, 24.4]R/V_r$ are specifically sampled in the transitional phase where mode growth and energy cascade happens, before reaching the statistically stable phase. Visualized as the energy transfer from higher to lower modes as turbulence develops. Columns are different trajectories, rows are compression methods, lines of varied colors are the k_y^{spec} at specific timesteps, and transparent lines are respective ground truth.

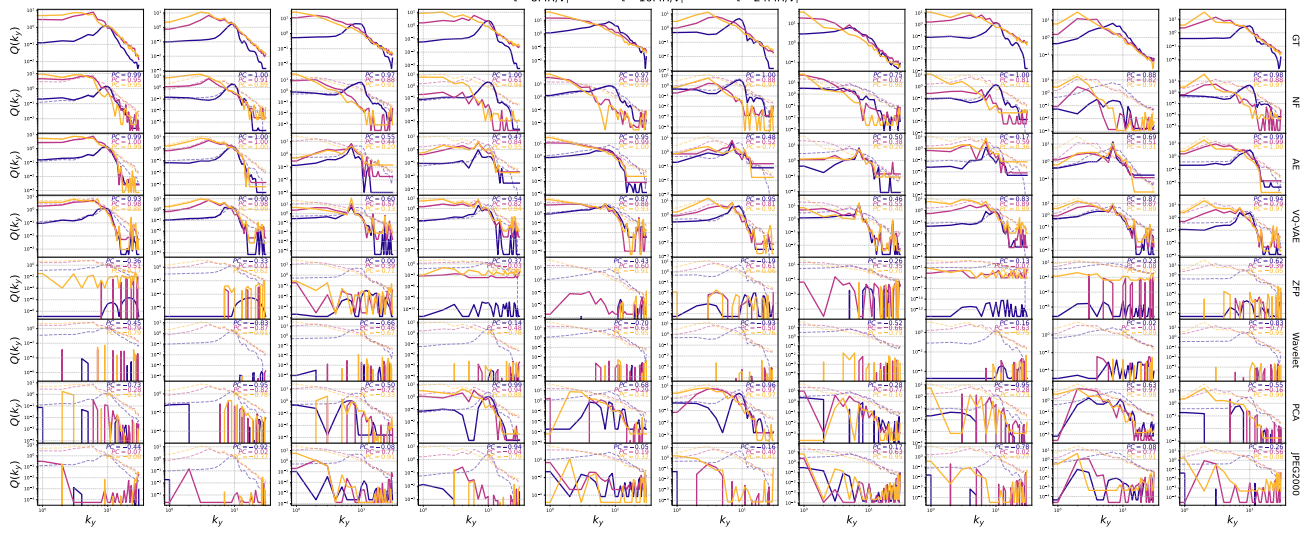


Figure 7. Extra models for the Q spectra (right Figure 4). The three time snapshots at $[8.4, 16.4, 24.4]R/V_r$ are specifically sampled in the transitional phase where mode growth and energy cascade happens, before reaching the statistically stable phase. Visualized as the energy transfer from higher to lower modes as turbulence develops. Columns are different trajectories, rows are compression methods, lines of varied colors are the Q^{spec} at specific timesteps, and transparent lines are respective ground truth.

Table 14. Timing details for neural and traditional compression, in seconds. GPU: single NVIDIA A40 (48GB), CPU: Intel Xeon Platinum 8168, 96 cores, 2.70GHz.

Model	Offline compute	Compress [s]	Decompress [s]	Device
NF	-	96.3	0.260	GPU
AE	$\sim 4 \times 60\text{h} + 28\text{h}$	0.377	0.023	GPU
VQ-VAE	$\sim 4 \times 60\text{h} + 28\text{h}$	0.425	0.027	GPU
ZFP	-	0.144	0.066	CPU
Wavelet	-	1.30	0.804	CPU
PCA	-	0.377	0.149	CPU
JPEG2000	-	4.17	0.261	CPU

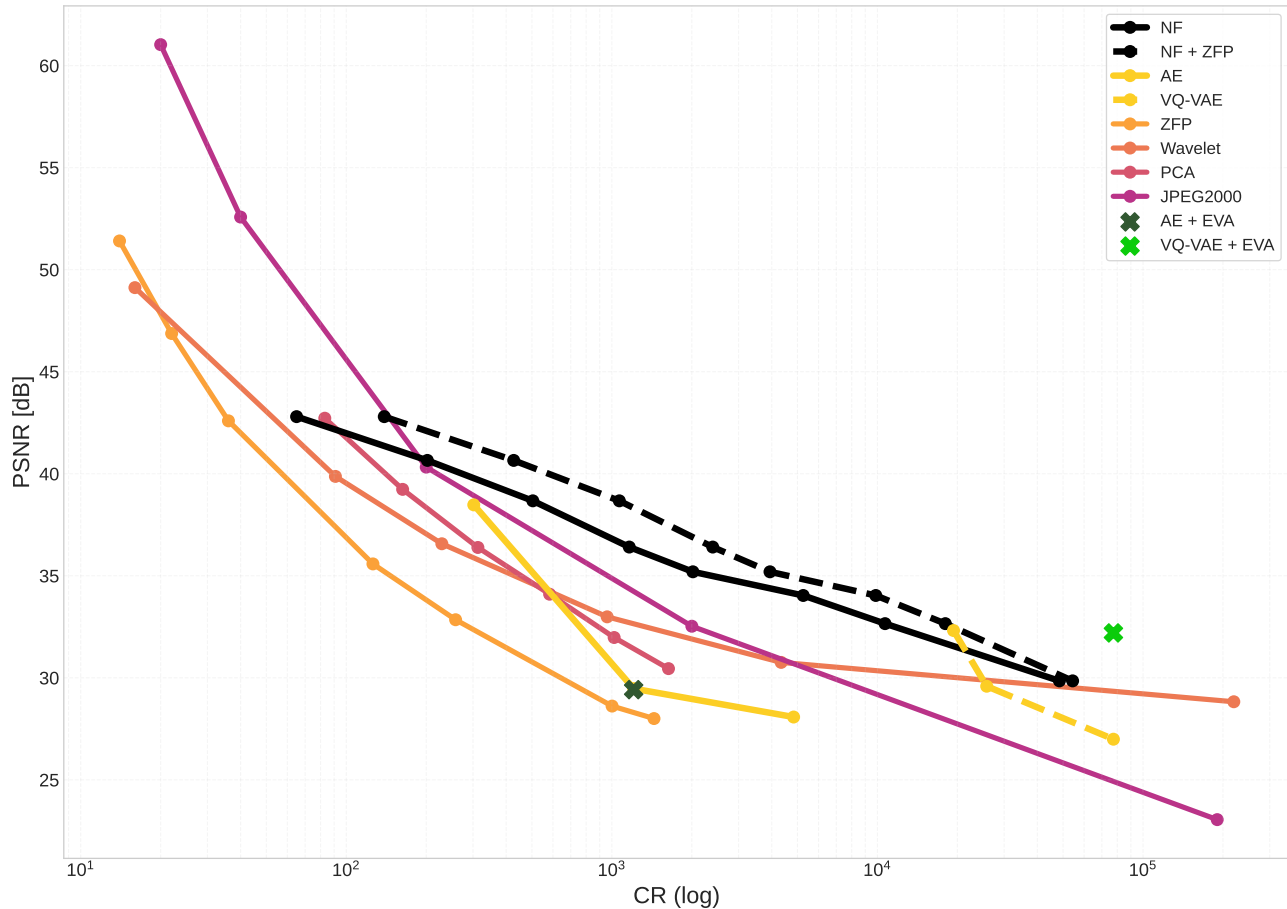


Figure 8. Full PSNR scaling plot with missing curves from Figure 2

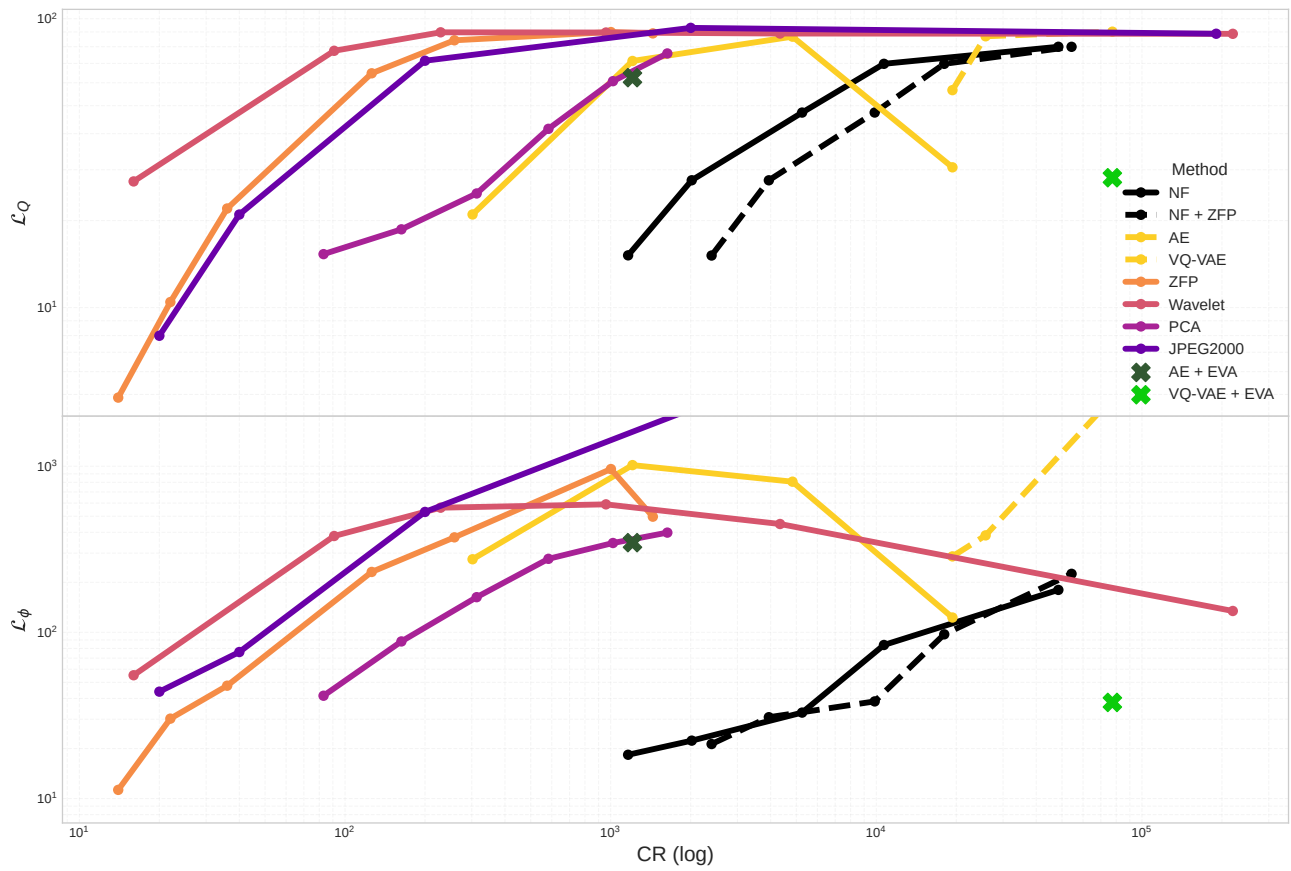


Figure 9. Full physics scaling plot with missing curves from Figure 3

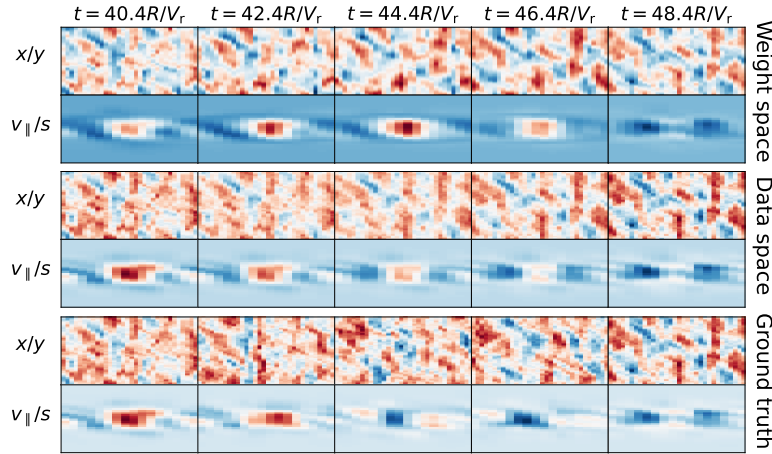

 Figure 10. Qualitative visualization of 5D f slices interpolated over time, between the two extremes at $t = 40.4R/V_r$ and $t = 48.4R/V_r$. Aspect ratio is set to 2 and does not represent the physical one.



Figure 11. Extra reconstructions for the 5D density function f . CR = $\sim 1,000\times$. Each row is a different trajectory at timestep 176.4 R/V_r . Columns match Figure 12. Aspect ratio is set to 2 and does not represent the physical one.

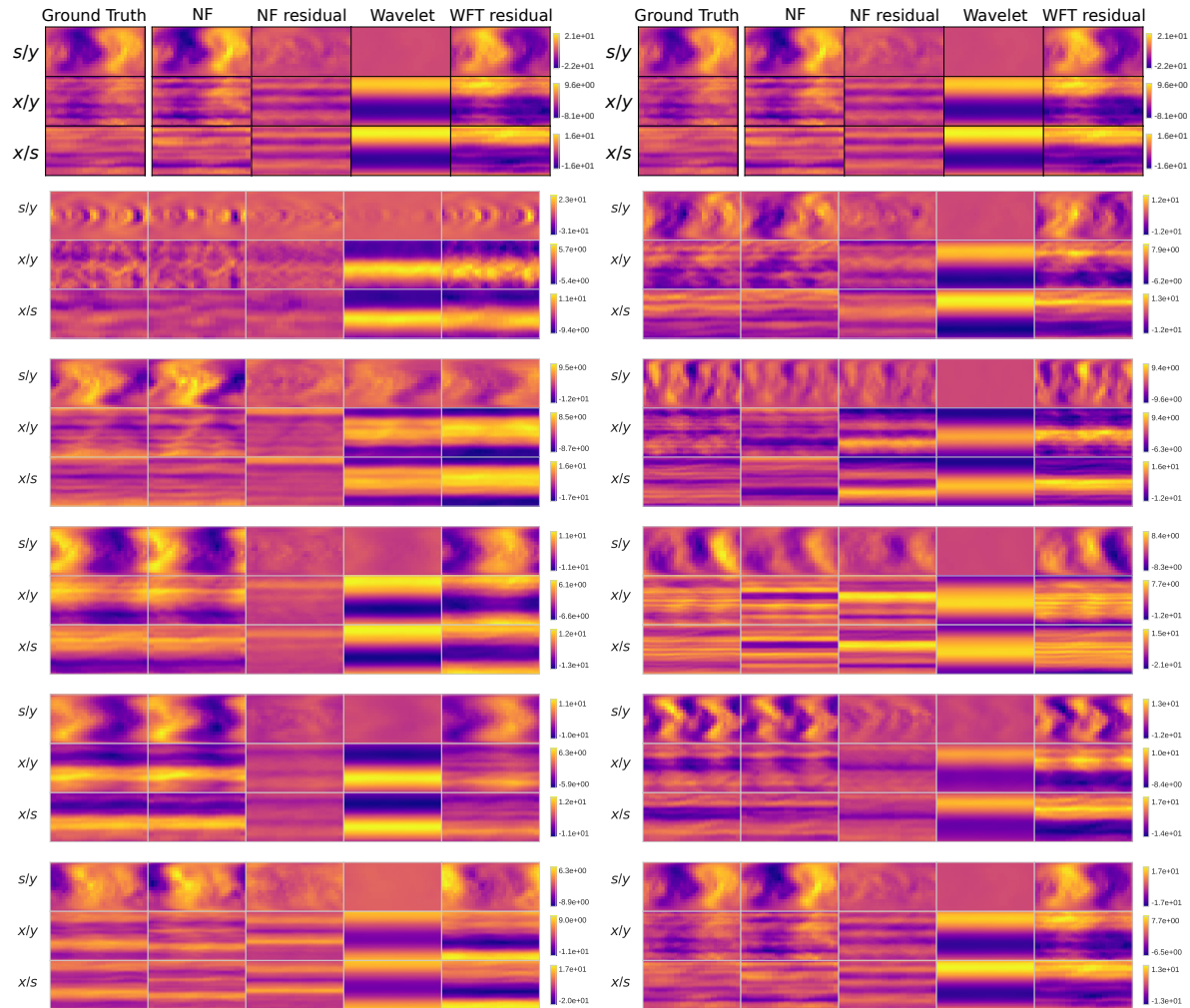


Figure 12. Extra reconstructions for the 3D electrostatic potential ϕ . CR = $\sim 1,000\times$. Each row is a different trajectory at timestep $176.4R/V_r$. Columns match Figure 11. Aspect ratio is set to 2 and does not represent the physical one.